

Plasmon-driven exciton formation in a non-equilibrium Fermi liquid

Rishi Acharya,^{1,2} Eli Gerber,³ Nina Bielinski,^{1,2} Hannah E. Aguirre,^{1,2} Younsik Kim,^{1,2} Camille Bernal-Choban,^{1,2} Gaurav Tenkila,^{1,4} Suhas Sheikh,^{1,4} Pranav Mahaadev,^{1,2} Faren Hoveyda-Marashi,^{1,2} Subhajit Roychowdhury,^{5,6} Chandra Shekhar,⁵ Claudia Felser,⁵ Peter Abbamonte,^{1,2} Benjamin J. Wieder,³ and Fahad Mahmood^{1,2,*}

¹*Department of Physics, The Grainger College of Engineering, University of Illinois Urbana-Champaign, Urbana, 61801 IL, USA*

²*Materials Research Laboratory, The Grainger College of Engineering, University of Illinois Urbana-Champaign, Urbana, 61801 IL, USA*

³*Institut de Physique Théorique, Université Paris-Saclay, CEA, CNRS, F-91191 Gif-sur-Yvette, France*

⁴*Institute of Condensed Matter Theory, University of Illinois at Urbana-Champaign, Urbana, IL 61801, USA*

⁵*Max Planck Institute for Chemical Physics of Solids, Dresden 01187, Germany*

⁶*Department of Chemistry, Indian Institute of Science Education and Research Bhopal, Bhopal 462066, India*

Collective modes in Fermi liquids are usually regarded as dissipation channels that relax electronic excitations through Landau damping. Whether such modes can instead mediate the formation of correlated electronic states under non-equilibrium conditions remains an open question. Here we show that, under optical photo-doping, a bulk plasmon can drive correlated inter-band transfer within a transient electronic continuum. Using time- and angle-resolved photoemission spectroscopy (Tr-ARPES) on EuCd_2As_2 supported by electronic structure calculations, we observe that at high excitation density, plasmons transfer energy from a weakly dispersing bulk band into unoccupied surface states. This bulk-to-surface redistribution stabilizes a long-lived, energy-localized spectral feature consistent with a Mahan exciton. Our results uncover a non-equilibrium regime of Fermi-liquid physics in which collective modes do not merely dissipate energy, but also stabilize correlated bound states.

Collective excitations in interacting Fermi systems are traditionally regarded as decay channels. In a conventional Fermi liquid, the plasmon branch lies outside the particle-hole continuum at long wavelengths, but enters it at finite momentum, where Landau damping transfers plasmon energy into electron-hole pairs (Fig. 1a) [1, 2]. This paradigm underlies the standard description of relaxation in metals, where collective modes redistribute electronic energy into particle-hole continua.

Such relaxation also extends to non-equilibrium settings: in optically excited metals and semiconductors, bosonic-mode-assisted inter- and intra-band scattering channels have been directly observed to transfer high-energy carriers into lower-energy electronic continua and bound states [3–5]. In these cases, the collective mode functions as an efficient pathway toward equilibration. Yet this established framework leaves open a fundamental question: can collective modes, rather than merely

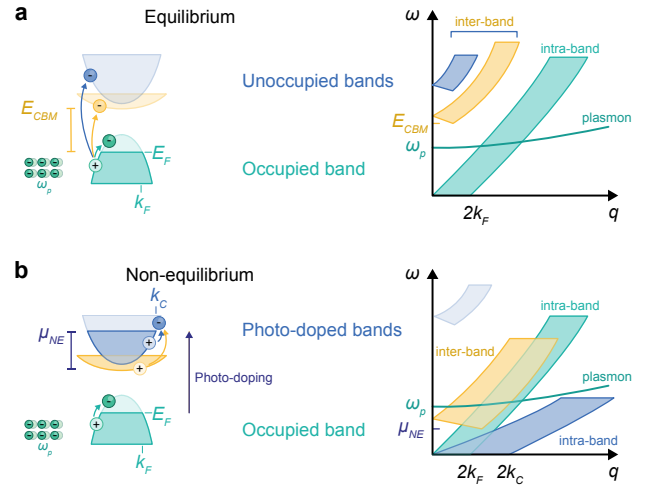


FIG. 1. Excitations of a Fermi liquid at and away from equilibrium: (a) Schematic depiction of the excitations of a Fermi liquid at equilibrium, represented as scattering processes along the occupied and unoccupied band dispersions (E vs k) (left) and as a spectrum showing the excitation energy ω as a function of the excitation wave vector q (right). In (a), E_F and k_F indicate the Fermi level and Fermi momentum, respectively. E_{CBM} indicates the energy minimum of the lower conduction band, measured relative to E_F , and ω_p denotes the energy of the plasmon. (b) Schematic depiction of the excitations of a Fermi liquid with a secondary chemical potential (μ_{NE}) photo-doped into a conduction band. In (b), μ_{NE} is measured relative to the bottom of the subset of photo-doped bands.

dissipating energy, actively drive the formation of correlated electronic states under non-equilibrium conditions?

In general, inter-band optical excitation generates a non-equilibrium carrier population that rapidly thermalizes to a secondary chemical potential within transiently filled bands [6]. The resulting inter- and intra-band excitation continua can extend to $\omega = 0$, overlapping with the plasmon branch (Fig. 1b). In this regime, collective modes need not act solely as sinks of energy; they may instead mediate interband transfer within the transient continuum.

* fahad@illinois.edu

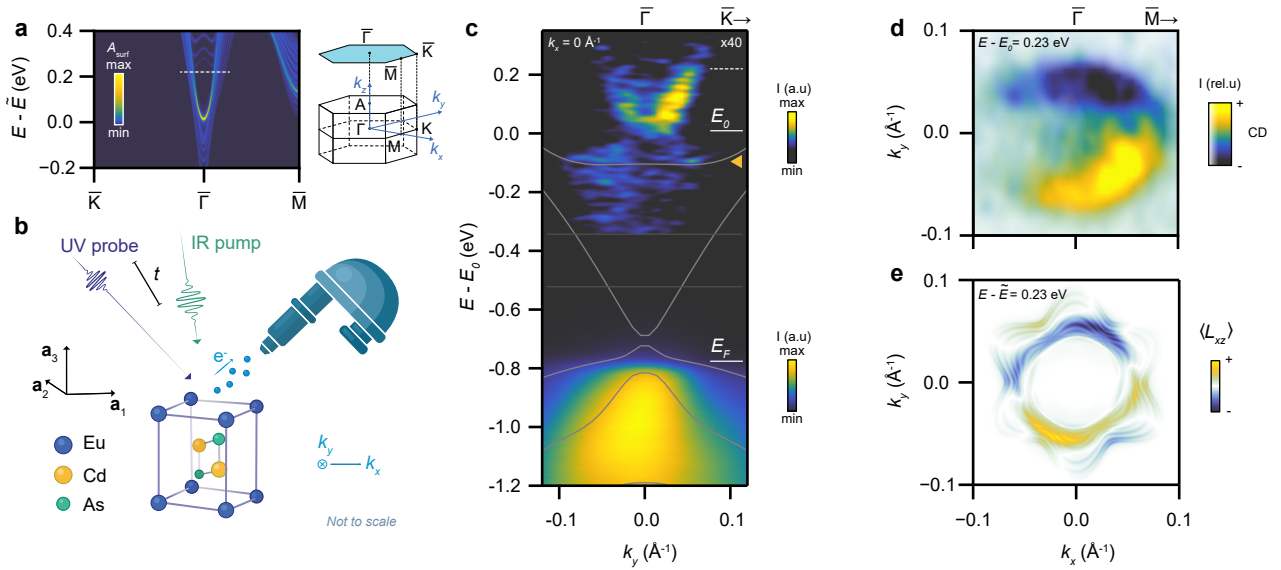


FIG. 2. Unoccupied band structure of EuCd_2As_2 : (a) (001)-surface spectral function of EuCd_2As_2 , obtained from *ab initio* density-functional theory (DFT) calculations in the paramagnetic (PM) state (Supplementary Information III A). The spectrum in (a), plotted in the blue shaded (001)-surface Brillouin zone (BZ) in the right schematic, consists of a nearly doubly degenerate pair of surface bands that coexist with the surface projections of the bulk conduction manifold; the surface band minimum lies at an energy that we denote as \tilde{E} . (b) Schematic of the time- and angle-resolved photoemission spectroscopy (Tr-ARPES) experiment. The UV probe and IR pump are incident along the (x, z) - and (y, z) -planes of the lab frame, both at 45° to the sample normal (the (001)-surface) and are *p*-polarized. In (b), the sample is aligned with $\bar{\Gamma} - \bar{M}$ along k_z . This measurement geometry probes both the (001)-surface and the bulk electronic structure at $k_z \approx 0$. (c) Time-integrated ($t - t_0 \in [0 \text{ ps}, 2 \text{ ps}]$) ARPES spectrum (E vs k_y) showing the occupied and unoccupied band structure of EuCd_2As_2 , with light gray lines showing the bulk band structure at $k_z = 0$ along $\bar{\Gamma} - \bar{K}$ from the PM-state DFT calculation, and with dark gray horizontal rules indicating where different scans were truncated to render the composite figure. Above the Fermi level E_F in (c), we observe a set of surface states whose dispersion closely matches the DFT-obtained surface states in (a) and whose minimum approximately lies at $E_0 \approx E_F + 0.8 \text{ eV}$ (Supplementary Information III B). Just below E_0 lies a bulk conduction band that is nondispersing at $\bar{\Gamma}$ to leading order (yellow triangle in (c)) in which exciton holes form. (d) A constant-energy cut of circular dichroism (CD-) ARPES measurements of the (001)-surface states taken along the dashed line in (c) ($E_0 + 0.23 \text{ eV}$, $\pm 30 \text{ meV}$ integration window) at t_0 , with a hue given by the difference between the ARPES intensities for opposite circular probe polarizations and a saturation set by the polarization-integrated photoemission intensity. (e) A constant-energy cut of the local atomic orbital angular momentum (OAM) of the (001)-surface states in the PM-phase DFT calculation in (a), taken at $\tilde{E} + 0.23 \text{ eV}$ (the dashed line in (a)) and projected along the incident axis of the probe ($\langle L_{xz} \rangle$, angled 45° between the bulk line $\bar{\Gamma} - \bar{A}$ and the surface and bulk line $\bar{\Gamma} - \bar{M}$ in the BZ in (a), see Supplementary Information III C). The Tr-ARPES measurements in this figure were taken at 20 K, below $T_C \approx 25 \text{ K}$ for the ferromagnetic phase, using 1.2 eV excitation of low fluence ($15 \mu\text{J}/\text{cm}^2$). Importantly, to facilitate comparison with the DFT calculations, we also performed the same measurements in the PM phase at 42 K, and observed qualitatively identical (CD-) ARPES spectra (Supplementary Information II).

Observing such an interaction channel in a bulk metal, however, is challenging. In three-dimensional systems, strong screening and the large phase space tend to smear interaction-enhanced features. Plasmons are heavily damped once they overlap with bulk continua, and competing scattering channels redistribute spectral weight broadly in momentum and energy. A more favorable setting would involve surface electronic bands interacting with a bulk plasmon. The reduced dimensionality of the surface suppresses phase space, weakens screening, and thus enhances interaction effects. Moreover, the near-field interaction between the dipole moment of a bulk collective mode in a low-carrier-density material and surface-localized conduction electrons is exponentially enhanced at zero-momentum transfer [7]. Thus,

in this configuration, a bulk plasmon could transfer energy to the more confined surface electron bands, giving rise to correlated features that can be spectrally resolved.

We here find that EuCd_2As_2 precisely provides the latter setting. As we demonstrate below, the electronic structure of EuCd_2As_2 hosts a bulk plasmon at an energy scale comparable to the separation between an unoccupied, weakly dispersing 3D bulk band and an unoccupied 2D surface state. Density-functional theory (DFT) calculations, presented below, establish the existence of these unoccupied surface states, motivating the experimental investigation of plasmon-mediated transfer between the bulk and surface in the non-equilibrium continuum. Using time- and angle-resolved photoemission spectroscopy (Tr-ARPES), we not only uncover this plasmon-mediated

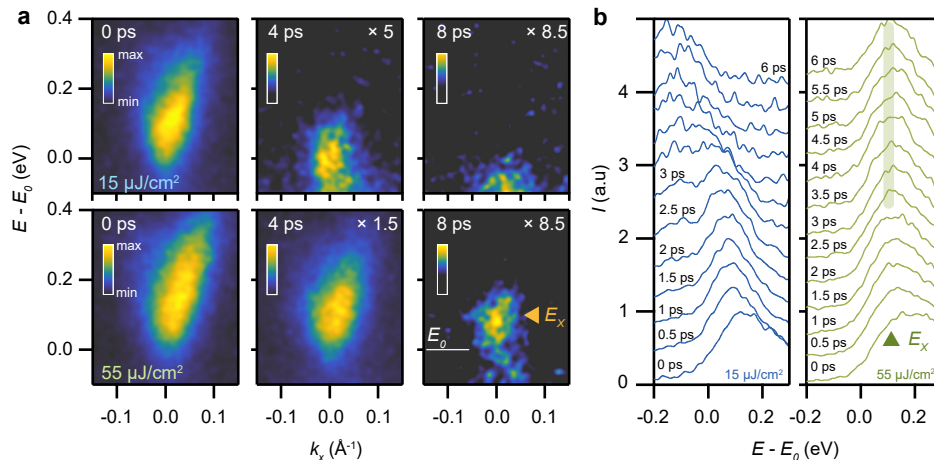


FIG. 3. **Population dynamics of the unoccupied surface states at representative excitation densities:** (a) ARPES spectra of the unoccupied band structure of EuCd_2As_2 at selected temporal delays after low-fluence (top row) and high-fluence (bottom row) excitation. (b) Energy distribution curves at various temporal delays after photo-excitation for low ($15 \mu\text{J}/\text{cm}^2$, left) and high ($55 \mu\text{J}/\text{cm}^2$, right) fluence photo-excitation, where the shaded region at E_X in the right panel is a guide to the eye. For the experimental data in this figure, the Tr-ARPES measurements were taken at 9.5 K using 1.5 eV excitation.

transfer, but also find that the reduced screening and constrained phase space of the surface stabilizes a long-lived, energy-localized spectral feature consistent with a Mahan exciton [8, 9]. Our results reveal a non-equilibrium regime of Fermi-liquid physics in which collective modes do not merely dissipate energy, but actively reshape electronic distributions by mediating correlated bulk-to-surface transfer.

EuCd_2As_2 has been previously characterized as semiconducting [10–12] or semimetallic throughout its magnetic phase diagram (Supplementary Information I and Ref. [13, 14]), with an antiferromagnetic phase reported below $T_N = 9$ K. In the samples used in this work, ferromagnetic (FM) order has been stabilized below $T_C = 25$ K through Eu vacancies [14]. Above T_C , EuCd_2As_2 lies in a paramagnetic (PM) state with bulk inversion (\mathcal{I}) and time-reversal (\mathcal{T}) symmetries. To analyze the bulk and surface electronic structure of EuCd_2As_2 , we performed *ab initio* (DFT) and Wannier-based tight-binding calculations of the electronic structure (Supplementary Information III A). For simplicity, and because our ARPES measurements produced qualitatively identical spectra both above and below T_C over the energy and momentum range probed in this study (Supplementary Information II), we performed our DFT calculations in the PM state. In our DFT-based calculations, we observe unoccupied (001)-surface bands that coexist with the projected continuum of unoccupied bulk states (the projected bulk conduction manifold) and exhibit an approximately hyperbolic dispersion with an energy minimum that we denote as \tilde{E} (Fig. 2a, see Supplementary Information III B). Through calculations of the (001)-surface spin texture in Supplementary Information III C, we find that the (001)-surface states in fact form a 2D Dirac cone with weak spin-orbit-coupling- (SOC-) driven

splitting away from $\mathbf{k} = \mathbf{0}$.

To understand the origin of the hyperbolic (001)-surface Dirac cone in Fig. 2a, we applied the group-theoretic methodology in Ref. [15] to compute the band topology at and away from E_F (Supplementary Information III D). Through this analysis, we identified a large range of electronic fillings – spanning from 5 electrons below intrinsic filling to 7 electrons above – at which EuCd_2As_2 in the PM state hosts 3D topological band-insulating gaps. We may hence associate the unoccupied (001)-surface states in Fig. 2a to a 3D topological band insulator phase at an electronic filling above E_F , which can be accessed by photo-doping experiments. In this sense, EuCd_2As_2 is reminiscent of the repeat-topological (RTopo) materials introduced in Ref. [15], which host topological gaps at and just below E_F . For example, in the RTopo material Bi_2Mg_3 , the topological band gap below E_F gives rise to topological surface resonance bands that coexist with the surface projections of the bulk valence manifold and are detectable in ARPES experiments [15–17]. The unoccupied (001)-surface states in EuCd_2As_2 and the associated topological band gaps above E_F can hence be viewed as a generalization of the concept of repeat-topology – originally introduced to predict topological boundary states accessible in equilibrium ARPES experiments at intrinsic filling – to topological surface conduction bands that are accessible by doping and Tr-ARPES experiments like those in the present study.

Having established the presence and energies of unoccupied surface states in EuCd_2As_2 , we now use Tr-ARPES to dynamically populate and resolve the surface bands. The geometry of the Tr-ARPES experiment is shown in Fig. 2b. In our measurements, *p*-polarized IR pulses at either 1.2 eV or at 1.5 eV excite inter-band tran-

sitions, after which we collect ARPES spectra using 6 eV photons with a variable delay from photo-excitation. In momentum space, the photon scattering plane coincides with a crystallographic mirror plane whose normal vector lies along k_y and is related to the BZ line $\bar{\Gamma}-\bar{K}$ in Fig. 2a by crystal symmetry. In Fig. 2c, we show an ARPES spectrum (E vs k_y) of the occupied and unoccupied bulk and surface band structure of EuCd_2As_2 . Below E_F at its equilibrium value (*i.e.*, at energies $E - E_0 < -0.8$ eV, where E_0 is assigned to the bottom of a bright electron-like unoccupied band), a broad valence band is visible, consistent with equilibrium synchrotron ARPES measurements [14] and bulk DFT calculations performed in the present study (gray lines, see Supplementary Information III A).

At 0.8 eV above E_F in Fig. 2c (*i.e.*, above E_0), we observe a sharp, nearly-linear (hyperbolic) electron-like feature, in strong agreement with the calculated surface spectral function in Fig. 2a. Slightly below E_0 in Fig. 2c, we observe a faint incoherent spectral weight, which we attribute to the bulk conduction band 0.75 eV above E_F , consistent with optical spectroscopy [10, 18] and high-energy electron energy loss spectroscopy (EELS) measurements (Supplementary Information IV). In Fig. 2d, we show circular dichroism ARPES (CD-ARPES) measurements of the (001)-surface states, which provide further details of their wavefunction textures, and exhibit excellent agreement with theoretical calculations of the surface-projected local (in real space) atomic-orbital contribution to the orbital angular momentum (Fig. 2e, see Supplementary Information III C).

We now investigate the dynamics of the photo-doped surface and bulk conduction bands under different photo-excitation fluences. In Fig. 3a, we plot ARPES spectra at several different time delays after excitation for two representative fluences. Immediately after excitation, a broad energy range is populated at both low and high fluence (left panels of the top and bottom rows of Fig. 3a, respectively). The photo-doped population above E_F (here, in the vicinity of the bottom of the surface band E_0 , see Fig. 2c) specifically corresponds to the non-equilibrium phase schematically depicted in Fig. 1b. At low fluence, only states at very low energies ($E < E_0$) remain occupied several picoseconds after excitation (Fig. 3a, top right). This is consistent with previous studies that mapped the unoccupied band structure in solids [6, 10, 19–21], in which long-lived populations above E_F were associated with the energy minima of unoccupied bulk bands. The momentum-integrated population at different times (Fig. 3b, left panel) can be fit using Fermi-Dirac distributions multiplied by linear densities of states (Supplementary Information V). We find that the resulting chemical potential at later delay times, $\mu(t \gg t_0)$, is largely independent of fluence, and that for 1.5 eV photon excitation, $\mu(t \gg t_0) \approx 100$ meV + E_0 .

Surprisingly, at high fluence (Fig. 3a, bottom row), a strong spectral weight persists at $E_X \equiv E_0 + 100$ meV, significantly above the surface band minimum E_0 (Sup-

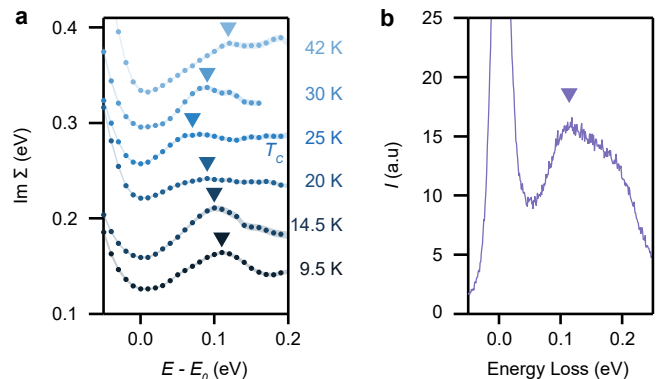


FIG. 4. Electron-plasmon coupling in the unoccupied conduction states: (a) The imaginary part of the self energy $\text{Im } \Sigma(E)$ of the unoccupied band structure, measured at various lattice temperatures under low fluence excitation ($15 \mu\text{J}/\text{cm}^2$) by 1.2 eV photons. The shaded colored regions in (a) indicate error bars for Lorentzian fits, and represent a 68% confidence interval. The blue triangles in (a) are guides to the eye to highlight the temperature dependence of the kink (derivative discontinuity). To generate (a), ARPES cuts were integrated over $t - t_0 \in [0 \text{ ps}, 2 \text{ ps}]$, and vertical offsets were added for clarity. (b) The momentum-integrated spectrum obtained from electron energy loss spectroscopy (EELS) at room temperature, showing a broad plasmon peak at 0.12 eV (purple triangle).

plementary Information VI), even after the populations at lower energies have largely decayed (Fig. 3a, bottom right). The strong energy localization of this long-lived spectral weight, and its qualitative absence for low fluence excitation, are shown in Fig. 3b. A clear transfer of spectral weight to lower energies over several picoseconds is visible for low fluence excitation (Fig. 3b, left), whereas for high fluence excitation (Fig. 3b, right), the spectrum after t_0 is distinctly sharpened at E_X relative to the initial hot electron distribution.

To identify the origin of this long-lived population at E_X , we examine the role of many-body interactions in the unoccupied bands. Under low fluence excitation, the imaginary part of the self energy, $\text{Im } \Sigma(E)$, extracted from ARPES linewidths [22, 23], shows a strong discontinuity in its derivative (a “kink”) at $E - E_0 \approx 150$ meV, which softens by roughly 70 meV around the PM to FM transition temperature $T_C = 25$ K (Fig. 4a). Such kinks arise from changes in quasiparticle lifetimes due to crossovers in scattering mechanisms, and thus here indicate strong coupling of the surface states in EuCd_2As_2 to a collective mode with the corresponding energy. Previous optical spectroscopy experiments [24, 25] and EELS measurements performed in this work (Fig. 4b) identify the relevant mode as the bulk plasmon. This suggests that as the electrons in the surface states cool, they transfer energy to a bath of plasmons [20, 26–28]. Thus, although the surface conduction band dynamics that we observe in EuCd_2As_2 differ sharply from previous Tr-ARPES studies of conduction band dynamics in

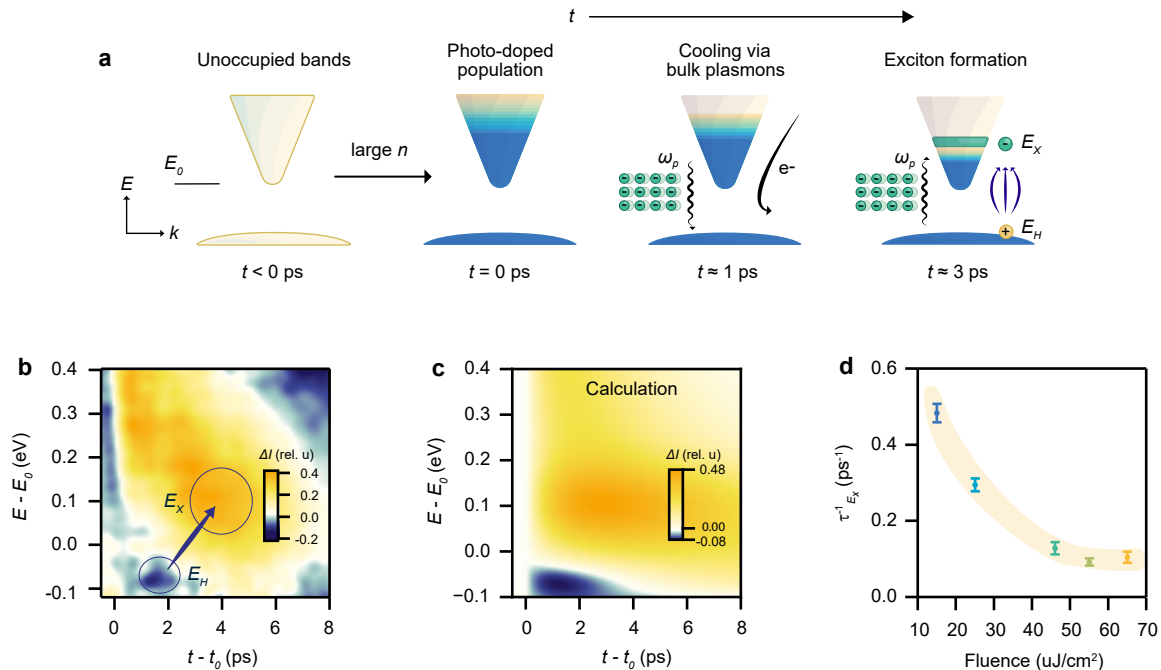


FIG. 5. **Plasmon-mediated exciton formation:** (a) Schematic of the dynamics of electrons excited into unoccupied surface states, showing the plasmon-mediated formation of Mahan excitons. (b) Difference between time traces for high ($55 \mu\text{J}/\text{cm}^2$) and low ($15 \mu\text{J}/\text{cm}^2$) excitation fluences, with the maximum intensity at each energy level for both fluences (reached approximately at t_0) normalized to 1. The superimposed arrow in (b) indicates the formation of holes and electrons associated with the exciton. (c) Theoretical calculation of plasmon-mediated exciton formation using a rate equation (Supplementary Information VII). (d) Decay rates at E_X for different excitation fluences; the yellow shaded region is a guide to the eye. The error bars in (d) represent a 68% confidence interval for exponential decay fits.

a broad set of materials [19, 29–31] – in which electron-electron scattering is the dominant interaction away from local band minima – the conduction band dynamics in EuCd_2As_2 can still be understood in the low-fluence regime through the conventional perspective of plasmons as a dissipation channel.

We posit that the role of plasmons is qualitatively different in the high-fluence regime, when the persistence of localized spectral weight at E_X arises due to a hot plasmon-driven inter-band transition, which creates a Mahan exciton with holes in the bulk conduction band just below E_0 (yellow triangle in Fig. 2c) and electrons in the surface conduction band, as shown schematically in Fig. 5a. A Mahan exciton forms with electrons at the effective Fermi level of an n -doped system, when hole densities are negligible due to valence degeneracy [8, 9]. We have previously noted that the chemical potential μ of the populations in the unoccupied surface bands cools to $\mu(t \gg t_0) \approx E_0 + 100 \text{ meV}$ (Supplementary Information V), which is equal to E_X . Moreover, our assessment of high valence degeneracy is supported by previous optical spectroscopy studies, which identify the bulk conduction band with a large mass at Γ in the energy range of the yellow triangle in Fig. 2c [10, 18], as well as our PM-state DFT calculations, which show a doubly degenerate

bulk band at approximately the same energy that is flat to leading order in three-dimensional k -space near Γ (Supplementary Information III A).

To test this interpretation, we first search for signatures of holes in the bulk conduction band after photo-excitation. This is challenging because, at equilibrium, all of the bulk and surface states involved in this scenario are unoccupied. We therefore identify holes in the bulk conduction band by comparing population dynamics between the excitonic and non-excitonic conditions, corresponding to high ($55 \mu\text{J}/\text{cm}^2$) and low ($15 \mu\text{J}/\text{cm}^2$) fluence, respectively. We show in Fig. 5b the difference between time traces for the high and low fluence excitations, with the maximum spectral weight at each energy for both fluences normalized to one. Strikingly, a relative depletion of spectral weight for high fluence accumulates at $E_H \equiv E_0 - 50 \text{ meV}$ during the first 2 ps (dark blue region in Fig. 5b). This indicates that the initial population decay at E_H is faster for high fluence excitation than for low fluence. Additionally, a substantially larger relative spectral weight at high fluence accumulates at E_X within a few picoseconds (gold region in Fig. 5b), consistent with the longer lifetime of the excitonic population.

We interpret these observations as evidence for an additional process – apparent only at high fluence – that

transfers spectral weight across the inter-band transition from E_H to E_X (blue arrow in Fig. 5b). Importantly, the energy difference $E_X - E_H$ is very similar to the plasmon energy previously identified in Fig. 4b, particularly considering that the plasmon energy increases with decreasing temperature [24], indicating that this transfer is plasmon-induced. The rate of such plasmon absorption should in turn scale quadratically with the excited carrier density, because the plasmons must first be excited by the relaxation of electrons in the unoccupied bands. Hence, the plasmon-induced transition from E_H to E_X is only dominant at high fluences, and excitons should not form in the low-fluence regime, consistent with our observations in Fig. 3a.

The contrast between the dynamics at low and high excitation fluences can be captured using a rate equation that treats the photo-excited population as relaxing via plasmon-mediated scattering, with an additional fluence-dependent channel that transfers spectral weight between electron and hole energies upon exciton formation. In Fig. 5c, we show numerical data generated using

this theoretical model, which are in close agreement with the experimental data in Fig. 5b (see Supplementary Information VII for complete calculation details). In this scenario (Fig. 5a), the exciton population lifetime is set by the electron-hole Coulomb energy, and is thus independent of the number of excitons generated. As a result, the population lifetime at E_X saturates with increasing fluence, consistent with the decay rates extracted at E_X in Fig. 5d.

To conclude, our observation of Mahan excitons motivates future studies to probe their spin polarization [32], electronic chirality [33], condensation [34, 35], and tunable binding energies [34]. From a broader perspective, our results point to a generalized form of carrier multiplication, in which the absorption of a photon creates multiple electron-hole excitations [36]. Moreover, due to their coherent near-field coupling to bulk modes, demonstrated in this study, surface non-equilibrium Fermi liquids constitute a powerful platform for collective interaction-driven phenomena inaccessible at thermal equilibrium, including phononic control of phase transitions [37, 38] and intrinsically driven Floquet phases [39].

-
- [1] Nozieres, P. & Pines, D. *The Theory Of Quantum Liquids* (CRC Press, Boca Raton, FL, 2018).
 - [2] Wehling, T. O., Black-Schaffer, A. M. & Balatsky, A. V. Dirac materials. *Advances in Physics* **63**, 1–76 (2014).
 - [3] Na, M. X. *et al.* Direct determination of mode-projected electron-phonon coupling in the time domain. *Science* **366**, 1231–1236 (2019).
 - [4] Schmitt, D. *et al.* Formation of moiré interlayer excitons in space and time. *Nature* **608**, 499–503 (2022).
 - [5] Madéo, J. *et al.* Directly visualizing the momentum-forbidden dark excitons and their dynamics in atomically thin semiconductors. *Science* **370**, 1199–1204 (2020).
 - [6] Gierz, I. *et al.* Snapshots of non-equilibrium Dirac carrier distributions in graphene. *Nature Materials* **12**, 1119–1124 (2013).
 - [7] Lee, J. J. *et al.* Interfacial mode coupling as the origin of the enhancement of Tc in FeSe films on SrTiO3. *Nature* **515**, 245–248 (2014).
 - [8] Mahan, G. D. Excitons in Degenerate Semiconductors. *Physical Review* **153**, 882 (1967).
 - [9] Mahan, G. D. Excitons in Metals: Infinite Hole Mass. *Physical Review* **163**, 612 (1967).
 - [10] Santos-Cottin, D. *et al.* EuCd2As2: A Magnetic Semiconductor. *Physical Review Letters* **131**, 186704 (2023).
 - [11] Nelson, R. A. *et al.* Revealing the EuCd2As2 Semiconducting Band Gap via n-Type La-Doping. *Chemistry of Materials* **36**, 7623–7632 (2024).
 - [12] Shi, Y. *et al.* Absence of Weyl nodes in EuCd2As2 revealed by the carrier density dependence of the anomalous Hall effect. *Physical Review B* **109** (2024).
 - [13] Ma, J. Z. *et al.* Spin fluctuation induced Weyl semimetal state in the paramagnetic phase of EuCd2As2. *Science Advances* **5**, eaaw4718 (2019).
 - [14] Roychowdhury, S. *et al.* Anomalous Hall Conductivity and Nernst Effect of the Ideal Weyl Semimetallic Ferromagnet EuCd2As2. *Advanced Science* **10**, 2207121 (2023).
 - [15] Vergniory, M. G. *et al.* All topological bands of all non-magnetic stoichiometric materials. *Science* **376** (2022).
 - [16] Chang, T.-R. *et al.* Realization of a Type-II Nodal-Line Semimetal in Mg3Bi2. *Advanced Science* **6**, 1800897 (2019).
 - [17] Zhou, T. *et al.* Experimental Evidence of Topological Surface States in Mg3Bi2 Films Grown by Molecular Beam Epitaxy. *Chinese Physics Letters* **36**, 117303 (2019).
 - [18] Wu, W. *et al.* The discovery of three-dimensional Van Hove singularity. *Nature Communications* **15**, 1–11 (2024).
 - [19] Puppini, M. *et al.* Excited-state band structure mapping. *Physical Review B* **105** (2022).
 - [20] Bao, C. *et al.* Population Inversion and Dirac Fermion Cooling in 3D Dirac Semimetal Cd3As2. *Nano Letters* **22**, 1138–1144 (2022).
 - [21] Fragkos, S. *et al.* Excited States Band Mapping and Ultrafast Nonequilibrium Dynamics in Topological Dirac Semimetal 1T-ZrTe2. *Nano Letters* (2024).
 - [22] Lanzara, A. *et al.* Evidence for ubiquitous strong electron-phonon coupling in high-temperature superconductors. *Nature* **412**, 510–514 (2001).
 - [23] Kaminski, A. & Fretwell, H. M. On the extraction of the self-energy from angle-resolved photoemission spectroscopy. *New Journal of Physics* **7**, 98 (2005).
 - [24] Wang, H. P., Wu, D. S., Shi, Y. G. & Wang, N. L. Anisotropic transport and optical spectroscopy study on antiferromagnetic triangular lattice EuCd2As2: An interplay between magnetism and charge transport properties. *Physical Review B* **94** (2016).
 - [25] Du, Y. *et al.* Comparative Raman spectroscopy of mag-

- netic topological material EuCd₂X₂ (X = P, As). *Journal of Physics: Condensed Matter* **34**, 224001 (2022).
- [26] Allen, P. B. Theory of thermal relaxation of electrons in metals. *Physical Review Letters* **59**, 1460 (1987).
- [27] Gierz, I., Link, S., Starke, U. & Cavalleri, A. Non-equilibrium Dirac carrier dynamics in graphene investigated with time- and angle-resolved photoemission spectroscopy. *Faraday Discussions* **171**, 311–321 (2014).
- [28] Sun, B. Y., Zhou, Y. & Wu, M. W. Dynamics of photoexcited carriers in graphene. *Physical Review B* **85**, 125413 (2012).
- [29] Sobota, J. A. *et al.* Direct Optical Coupling to an Unoccupied Dirac Surface State in the Topological Insulator Bi₂Se₃. *Physical Review Letters* **111**, 136802 (2013).
- [30] Sobota, J. A. *et al.* Ultrafast electron dynamics in the topological insulator Bi₂Se₃ studied by time-resolved photoemission spectroscopy. *Journal of Electron Spectroscopy and Related Phenomena* **195**, 249–257 (2014).
- [31] Tanimura, H., Kanasaki, J. & Tanimura, K. Ultrafast scattering processes of hot electrons in InSb studied by time- and angle-resolved photoemission spectroscopy. *Physical Review B* **91**, 045201 (2015).
- [32] Mori, R. *et al.* Spin-polarized spatially indirect excitons in a topological insulator. *Nature* **614**, 249–255 (2023).
- [33] Kung, H. H. *et al.* Observation of chiral surface excitons in a topological insulator Bi₂Se₃. *Proceedings of the National Academy of Sciences of the United States of America* **116**, 4006–4011 (2019).
- [34] Pertsova, A. & Balatsky, A. V. Excitonic instability in optically pumped three-dimensional Dirac materials. *Physical Review B* **97**, 075109 (2018).
- [35] Mori, R. *et al.* Possible evidence of excitonic condensation in a topological insulator. *Proceedings of the National Academy of Sciences of the United States of America* **122**, e2422667122 (2025).
- [36] Nozik, E. P. & MEGEEH, A. J. Nanophotonics: Making the most of photons. *Nature Nanotechnology* **4**, 548–549 (2009).
- [37] Rini, M. *et al.* Control of the electronic phase of a manganese by mode-selective vibrational excitation. *Nature* **449**, 72–74 (2007).
- [38] Basov, D. N., Averitt, R. D. & Hsieh, D. Towards properties on demand in quantum materials. *Nature Materials* **16**, 1077–1088 (2017).
- [39] Hübener, H., De Giovannini, U. & Rubio, A. Phonon Driven Floquet Matter. *Nano Letters* **18**, 1535–1542 (2018).
- [40] Giannozzi, P. *et al.* QUANTUM ESPRESSO: a modular and open-source software project for quantum simulations of materials. *Journal of Physics: Condensed Matter* **21**, 395502 (2009).
- [41] Giannozzi, P. *et al.* Advanced capabilities for materials modelling with Quantum ESPRESSO. *Journal of Physics: Condensed Matter* **29**, 465901 (2017).
- [42] Giannozzi, P. *et al.* Quantum ESPRESSO toward the exascale. *The Journal of Chemical Physics* **152**, 154105 (2020).
- [43] Dudarev, S. L., Botton, G. A., Savrasov, S. Y., Humphreys, C. J. & Sutton, A. P. Electron-energy-loss spectra and the structural stability of nickel oxide: An LSDA+U study. *Physical Review B* **57**, 1505–1509 (1998).
- [44] Pizzi, G. *et al.* Wannier90 as a community code: new features and applications. *Journal of Physics: Condensed Matter* **32**, 165902 (2020).
- [45] Marzari, N. & Vanderbilt, D. Maximally localized generalized Wannier functions for composite energy bands. *Physical Review B* **56**, 12847 (1997).
- [46] Souza, I., Marzari, N. & Vanderbilt, D. Maximally localized Wannier functions for entangled energy bands. *Physical Review B* **65**, 035109 (2001).
- [47] Zhi, G.-X., Xu, C., Wu, S.-Q., Ning, F. & Cao, C. WannSymm: A symmetry analysis code for Wannier orbitals. *Computer Physics Communications* **271**, 108196 (2022).
- [48] Sinisa Coh & David Vanderbilt. Python Tight-Binding (PythTB) Package (2022).
- [49] Vig, S. *et al.* Measurement of the dynamic charge response of materials using low-energy, momentum-resolved electron energy-loss spectroscopy (M-EELS). *SciPost Phys* **3**, 26 (2017).
- [50] Jo, N. H. *et al.* Manipulating magnetism in the topological semimetal EuCd₂As₂. *Physical Review B* **101**, 140402 (2020).
- [51] Acharya, R. *et al.* Data for "Plasmon-driven exciton formation in a non-equilibrium Fermi liquid". URL https://doi.org/10.13012/B2IDB-5098803_v1.
- [52] Soh, J.-R. *et al.* Ideal Weyl semimetal induced by magnetic exchange. *Physical Review B* **100**, 201102 (2019).
- [53] Cuono, G., Sattigeri, R. M., Autieri, C. & Dietl, T. Ab initio overestimation of the topological region in Eu-based compounds. *Physical Review B* **108**, 075150 (2023).
- [54] Neil Ashcroft & David Mermin. *Solid State Physics* (Saunders College Publishing, 1976), 1 edn.
- [55] Ponzoni, S. *et al.* Dirac Bands in the Topological Insulator Bi₂Se₃ Mapped by Time-Resolved Momentum Microscopy. *Advanced Physics Research* **2** (2023).
- [56] Sidilkover, I. *et al.* Reexamining circular dichroism in photoemission from a topological insulator. *Physical Review Research* **7**, 33027 (2025).
- [57] Schellenberg, I., Pfannenschmidt, U., Eul, M., Schwickert, C. & Pöttgen, R. A 121Sb and 151Eu Mössbauer Spectroscopic Investigation of EuCd₂X₂ (X = P, As, Sb) and YbCd₂Sb₂. *Zeitschrift für anorganische und allgemeine Chemie* **637**, 1863–1870 (2011).
- [58] Bergerhoff, G., Hundt, R., Sievers, R. & Brown, I. D. The inorganic crystal structure data base. *Journal of Chemical Information and Computer Sciences* **23**, 66–69 (1983).
- [59] Elcoro, L. *et al.* Magnetic topological quantum chemistry. *Nature Communications* **12**, 5965– (2021).
- [60] Xu, Y. *et al.* High-throughput calculations of magnetic topological materials. *Nature* **586**, 702–707 (2020).
- [61] Blöchl, P. E. Projector augmented-wave method. *Physical Review B* **50**, 17953–17979 (1994).
- [62] Kresse, G. & Joubert, D. From ultrasoft pseudopotentials to the projector augmented-wave method. *Physical Review B* **59**, 1758–1775 (1999).
- [63] Perdew, J. P., Burke, K. & Ernzerhof, M. Generalized Gradient Approximation Made Simple. *Physical Review Letters* **77**, 3865–3868 (1996).
- [64] Dal Corso, A. Pseudopotentials periodic table: From H to Pu. *Computational Materials Science* **95**, 337–350 (2014).
- [65] Vafek, O. & Vishwanath, A. Dirac fermions in solids: From high-T_c cuprates and graphene to topological insulators and Weyl semimetals. *Annual Review of Condensed*

- Matter Physics* **5**, 83–112 (2014).
- [66] Wieder, B. J. & Kane, C. L. Spin-orbit semimetals in the layer groups. *Physical Review B* **94**, 155108 (2016).
- [67] Watanabe, H., Po, H. C., Vishwanath, A. & Zaletel, M. Filling constraints for spin-orbit coupled insulators in symmorphic and nonsymmorphic crystals. *PNAS* **112**, 14551–14556 (2015).
- [68] Wu, Q., Zhang, S., Song, H.-F., Troyer, M. & Soluyanov, A. A. WannierTools: An open-source software package for novel topological materials. *Computer Physics Communications* **224**, 405–416 (2018).
- [69] Saito, K., Sawahata, H., Komine, T. & Aono, T. Tight-binding theory of surface spin states on bismuth thin films. *Physical Review B* **93**, 41301 (2016).
- [70] Fang, C., Gilbert, M. J., Xu, S.-Y., Bernevig, B. A. & Hasan, M. Z. Theory of quasiparticle interference in mirror-symmetric two-dimensional systems and its application to surface states of topological crystalline insulators. *Physical Review B* **88**, 125141 (2013).
- [71] Mahan, G. D. *Many-Particle Physics*. Physics of Solids and Liquids (Springer US, 1990).
- [72] Shockley, W. On the Surface States Associated with a Periodic Potential. *Physical Review* **56**, 317 (1939).
- [73] Lee, W. *et al.* Layer-by-layer disentanglement of Bloch states. *Nature Physics* **19**, 950–955 (2023).
- [74] Wu, X. *et al.* Distinct Topological Surface States on the Two Terminations of MnBi₄Te₇. *Physical Review X* **10**, 031013 (2020).
- [75] Kohsaka, Y. *et al.* Spin-orbit scattering visualized in quasiparticle interference. *Physical Review B* **95**, 115307 (2017).
- [76] Chang, G. *et al.* Unconventional Chiral Fermions and Large Topological Fermi Arcs in RhSi. *Phys. Rev. Lett.* **119**, 206401 (2017).
- [77] Schirmann, J., Grushin, A. G. & Wieder, B. J. Geometry-Enforced Topological Chiral Fermions in Amorphous Chiral Metals. *arXiv arXiv:2512.19791* (2025).
- [78] Yu, R., Qi, X. L., Bernevig, A., Fang, Z. & Dai, X. Equivalent expression of Z_2 topological invariant for band insulators using the non-Abelian Berry connection. *Phys. Rev. B* **84**, 75119 (2011).
- [79] Benalcazar, W. A., Bernevig, B. A. & Hughes, T. L. Electric multipole moments, topological multipole moment pumping, and chiral hinge states in crystalline insulators. *Phys. Rev. B* **96**, 245115 (2017).
- [80] Lin, K. S. *et al.* Spin-resolved topology and partial axion angles in three-dimensional insulators. *Nature Communications* **15** (2024).
- [81] Hasan, M. Z. & Kane, C. L. Colloquium: Topological insulators. *Reviews of Modern Physics* **82**, 3045–3067 (2010).
- [82] Wieder, B. J. *et al.* Topological materials discovery from crystal symmetry. *Nature Reviews Materials* **7**, 196–216 (2022).
- [83] Park, S. R., Kim, C. H., Yu, J., Han, J. H. & Kim, C. Orbital-angular-momentum based origin of rashba-type surface band splitting. *Physical Review Letters* **107**, 156803 (2011).
- [84] Park, S. R. *et al.* Chiral Orbital-Angular Momentum in the Surface States of Bi₂Se₃. *Physical Review Letters* (2012).
- [85] Wang, Y. & Gedik, N. Circular dichroism in angle-resolved photoemission spectroscopy of topological insulators. *physica status solidi – Rapid Research Letters* **7**, 64–71 (2013).
- [86] Yen, Y. *et al.* Controllable orbital angular momentum monopoles in chiral topological semimetals. *Nature Physics* **20**, 1912–1918 (2024).
- [87] Griffiths, D. J. *Introduction to Quantum Mechanics* (Cambridge University Press, 2016).
- [88] Muggli, J. Cubic harmonics as linear combinations of spherical harmonics. *Zeitschrift für angewandte Mathematik und Physik ZAMP* **23**, 311–317 (1972).
- [89] McQuarrie, D. A. & Simon, J. D. *Physical Chemistry: A Molecular Approach* (University Science Books, 1997).
- [90] Sakurai, J. J. & Napolitano, J. *Modern Quantum Mechanics* (Cambridge University Press, 2017).
- [91] Bradlyn, B. *et al.* Topological quantum chemistry. *Nature* **547**, 298–305 (2017).
- [92] Kruthoff, J., de Boer, J., van Wezel, J., Kane, C. L. & Slager, R.-J. Topological Classification of Crystalline Insulators through Band Structure Combinatorics. *Phys. Rev. X* **7**, 41069 (2017).
- [93] Po Hoi Chun, Vishwanath, A. & Watanabe Haruki. Symmetry-based indicators of band topology in the 230 space groups. *Nature Communications* **8**, 50 (2017).
- [94] Song Zhida, Zhang, T., Fang Zhong & Fang Chen. Quantitative mappings between symmetry and topology in solids. *Nature Communications* **9**, 3530 (2018).
- [95] Khalaf, E., Po, H. C., Vishwanath, A. & Watanabe, H. Symmetry Indicators and Anomalous Surface States of Topological Crystalline Insulators. *Phys. Rev. X* **8**, 31070 (2018).
- [96] Kresse, G. & Furthmüller, J. Efficiency of ab-initio total energy calculations for metals and semiconductors using a plane-wave basis set. *Computational Materials Science* **6**, 15 – 50 (1996).
- [97] Kresse, G. & Furthmüller, J. Efficient iterative schemes for ab initio total-energy calculations using a plane-wave basis set. *Phys. Rev. B* **54**, 11169–11186 (1996).
- [98] Gao, J., Wu, Q., Persson, C. & Wang, Z. Irvsp: To obtain irreducible representations of electronic states in the VASP. *Computer Physics Communications* **261**, 107760 (2021).
- [99] Aroyo, M. I. *et al.* Bilbao Crystallographic Server: I. Databases and crystallographic computing programs. *Zeitschrift für Kristallographie* **221**, 15–27 (2006).
- [100] Aroyo, M. I., Kirov, A., Capillas, C., Perez-Mato, J. M. & Wondratschek, H. Bilbao Crystallographic Server. II. Representations of crystallographic point groups and space groups. *Acta Crystallographica Section A* **62**, 115–128 (2006).
- [101] Aroyo, M. I. *et al.* Crystallography online: Bilbao Crystallographic Server. *Bulgarian Chemical Communications* **43**, 183–197 (2011).
- [102] Vergniory, M. G. *et al.* A complete catalogue of high-quality topological materials. *Nature* **566**, 480–485 (2019).
- [103] Bradley, C. J. & Cracknell, A. P. *The Mathematical Theory of Symmetry in Solids* (Oxford University Press, 1972).
- [104] Togo, A., Shinohara, K. & Tanaka, I. Spglib: a software library for crystal symmetry search. *Science and Technology of Advanced Materials: Methods* **4** (2024).
- [105] Seitz, F. The symmetry of crystals. *Annals of Mathematics* **37**, 17–84 (1936).
- [106] Wieder, B. J. *et al.* Wallpaper fermions and the nonsym-

- morphic Dirac insulator. *Science* **361**, 246–251 (2018).
- [107] Fu, L. & Kane, C. L. Topological insulators with inversion symmetry. *Phys. Rev. B* **76**, 45302 (2007).
- [108] Fu, L., Kane, C. L. & Mele, E. J. Topological Insulators in Three Dimensions. *Phys. Rev. Lett.* **98**, 106803 (2007).
- [109] Boschini, F., Zonno, M. & Damascelli, A. Time-resolved ARPES studies of quantum materials. *Reviews of Modern Physics* **96**, 015003 (2024).
- [110] Damascelli, A., Hussain, Z. & Shen, Z. X. Angle-resolved photoemission studies of the cuprate superconductors. *Reviews of Modern Physics* **75**, 473 (2003).
- [111] Zhu, X. *et al.* A holistic view of the dynamics of long-lived valley polarized dark excitonic states in monolayer WS₂. *Nature Communications* **16**, 6385– (2025).

METHODS

Time- and Angle-Resolved Photoemission Spectroscopy Measurements

The Tr-ARPES experiments were performed in the home lab at the University of Illinois, Urbana-Champaign. The fifth harmonic (6 eV) of the 1.2 eV (1030 nm) output of a Yb:KGW amplified laser (Pharos, Light Conversion) was used as the probe. The linearly polarized probe was transmitted through a quarter waveplate for CD-ARPES measurements. The IR excitation pulses of 1.2 eV (1000 nm) and 1.5 eV (825 nm) were provided by an OPA (Orpheus, Light Conversion) pumped by the same Yb:KGW laser. The samples were cleaved at 9.5 K at a base pressure better than 1×10^{-10} mB. Measurements were performed using a hemispherical analyzer (DA-30L, Scienta Omicron) equipped with a deflection mode to observe dispersion along both in-plane axes without rotation of the sample. The sample crystal axes were aligned using the measured Fermi surface. The energy resolution (measured through Fermi edge broadening on Bi₂Se₃) was better than 10 meV. The momentum resolution was better than 0.02 \AA^{-1} . The overall temporal resolution of the system (measured by cross-correlation on unoccupied topological surface states of Bi₂Se₃) was set at 200 fs.

First-Principles and Surface State Calculations

We performed the *ab initio* calculations of the electronic structure of the PM phase of EuCd₂As₂ within the density-functional theory (DFT) framework, as implemented in the Quantum Espresso software package [40–42]. The calculations included fully relativistic spin-orbit coupling (SOC) in the noncollinear scheme. In this setup, when no initial magnetic moments are specified, the self-consistent cycle converges to a nonmagnetic, \mathcal{T} -invariant solution. To properly localize the half-filled Eu 4*f* orbitals and improve the overall accuracy of the PM-state band structure, a Hubbard *U* correction of $U = 5 \text{ eV}$

on the Eu sites was implemented within the GGA+*U* scheme [43]. To analyze the spectral and topological properties of the PM state, we used maximally localized Wannier functions [44–46] to construct a tight-binding model using the Eu 5*d* and 4*f*, Cd 5*s*, and As 4*p* orbitals with SOC, and symmetrized the model [47] using the crystal symmetries in SG 164 ($P\bar{3}m1$) and time-reversal symmetry. To study the (001)-surface states, we constructed a finite slab model using the PythTB software package [48] with the Wannier model as input. Within the slab model, we then computed the surface spectral function and spin and orbital angular momentum textures using surface Green’s functions (see Supplementary Information III for complete DFT calculation details).

Electron Energy Loss Spectroscopy Measurements

To increase scattering intensity for momentum-resolved electron energy loss spectroscopy (M-EELS) measurements, five single crystals of FM-EuCd₂As₂ from the same batch used for Tr-ARPES measurements were roughly vertically co-aligned on an oxygen free high-conductivity copper puck. The samples were secured with Ag-epoxy (EPOTEK H2OE) cured at 150°C for an hour. Custom posts were mounted on top of the samples using the same epoxy. After preparation, the samples were cleaved in a UHV chamber ($\sim 5 \times 10^{-10}$ Torr) at room temperature and transferred into the M-EELS measurement chamber held at $\sim 7 \times 10^{-11}$ Torr.

The M-EELS experiments were performed in a reflection geometry using a modified high-resolution EELS spectrometer (ELS5000, LK Technologies) with the sample placed in an eucentric cryogenic three-circle goniometer [49]. The samples were placed such that the out-of-plane momentum transfer was along the *c*-axis. An incident energy of 50 eV with an energy resolution of 6.6 meV was used throughout. Due to the rough alignment of the individual crystals, the momentum in the scattering plane was considered integrated (*i.e.*, a single value of *q* contains information summed over the full Brillouin zone).

Sample Synthesis

The EuCd₂As₂ samples were grown using a salt-flux method, with high-quality elemental Eu, Cd, and As pieces, and an equimolar ratio of NaCl and KCl. The growth method, as well as sample characterization through transport, scanning tunneling microscopy, and synchrotron ARPES measurements, are described in Ref. [14]. We note that the salt flux growth method used for the samples in this work (as opposed to the Sn flux method more commonly used for the growth of EuCd₂As₂) leads to approximately 1% Eu vacancies, which results in FM order appearing below $T_C \sim 25 \text{ K}$

(as opposed to antiferromagnetic ordering below $T_N \sim 9$ K) [50].

Acknowledgments: We thank V. Madhavan, M. Knudtson, M. Vergniory, and J. Goldberger for insightful discussions. R.A., N.B., H.E.A., Y.K., P.M., and F.M. acknowledge support from NSF Career Award No. DMR-2144256 and from the EPiQS program of the Gordon and Betty Moore Foundation, Grant No. GBMF11069. C.B.-C., F.H.-M., and P.A. acknowledge support from the Center for Quantum Sensing and Quantum Materials, an Energy Frontier Research Center funded by the U.S. Department of Energy (DOE), Office of Science, Basic Energy Sciences (BES), under Award No. DE-SC0021238, as well as additional support from the EPiQS program of the Gordon and Betty Moore Foundation, Grant No. GBMF9452. B.J.W. and E.G. acknowledge support from the European Union’s Horizon Europe research and innovation program (ERC-StG-101117835-TopoRosetta), ANR PIA funding (ANR-20-IDEES-0002), and CNRS IRP Project NP-Strong. B.J.W. and E.G. further acknowledge the Laboratoire de Physique des Solides, Orsay for hosting during the preparation of this work. Sample characterization was carried out in part in the Materials Research Laboratory Central Research Facilities, University of Illinois. The first-principles calculations for this work were performed using the CCRT High-Performance Computing (HPC) facility under the Grant CCRT2025-gerbere awarded by the Fundamental Research Division (DRF) of the CEA.

Author contributions: R.A., N.B., H.E.A., Y.K., and P.M. performed the Tr-ARPES experiments and the corresponding data analysis. E.G. and B.J.W. developed the theoretical understanding through *ab initio* calculations of the bulk and surface electronic structure. G.T. and S.S. provided crucial insights into electronic dynamics. C.B.-C., F.H.-M., and P.A. performed the EELS experiments. S.R., C.S., and C.F. synthesized and characterized the samples for the Tr-ARPES experiments. R.A., E.G., B.J.W., and F.M. wrote the manuscript with input from all of the authors. F.M. conceived and supervised this project.

Competing interests: The authors declare no competing interests.

Data availability: The data in this Article are available via Illinois Data Bank [51].

Supplementary Information for “Plasmon-driven exciton formation in a non-equilibrium Fermi liquid”

CONTENTS

I. Evidence for a Weyl semimetal phase in ferromagnetic EuCd_2As_2	12
II. Temperature-independence of the surface-state dispersion and circular dichroism ARPES measurements	14
III. First-Principles Calculations	15
A. First-principles calculations and Wannier tight-binding model of the paramagnetic state of EuCd_2As_2	15
B. Surface spectral function calculation details	17
C. Spin and orbital textures of the (001)-surface states	20
D. Topological classification and band topology above the Fermi level in EuCd_2As_2	27
IV. Estimating the position of the bulk conduction band with electron energy loss spectroscopy (EELS)	31
V. Extracting and fitting transient electronic temperatures and dispersions from Tr-ARPES data	32
VI. Absence of time-dependent photovoltage shifts	34
VII. Rate equation modeling of plasmon-mediated exciton formation	35

I. EVIDENCE FOR A WEYL SEMIMETAL PHASE IN FERROMAGNETIC EuCd_2As_2

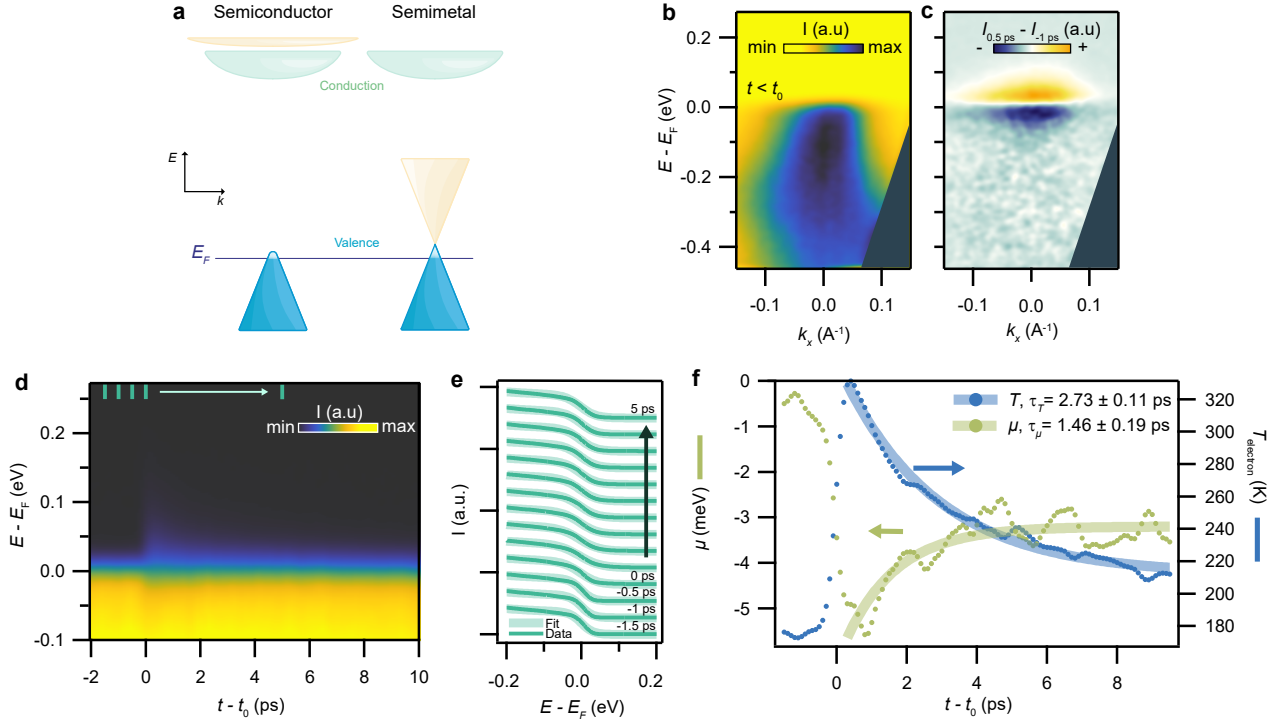


FIG. S1. **Evidence for a Weyl semimetal phase in ferromagnetic EuCd_2As_2 :** (a) Schematics of the competing descriptions of the bulk electronic band structure of EuCd_2As_2 near the Fermi energy (E_F) in the ferromagnetic (FM) state. (b) $E - E_F$ vs k_x spectra obtained from our ARPES measurements before photo-excitation, at a lattice temperature approximately at the FM transition $T_C \approx 25$ K. (c) Difference plot showing the equilibrium occupation of (b) subtracted from the time-integrated occupation between 0 and 1 ps after photo-excitation by 1.2 eV photons at low fluence ($15 \mu\text{J}/\text{cm}^2$). (d) Time trace corresponding to the spectra shown in (b) and (c). (e) Waterfall plot showing Fermi-Dirac fits (each convolved with a 10 meV Gaussian resolution function) for the electron distribution curves (EDCs) from the time trace shown in (d), taken at the times indicated by the vertical green bars at the top of (d). For the Fermi-Dirac fits in (e), we take the density of states to vary quadratically around $E - E_F = 50$ meV, and include a constant background offset attributed to impurities and pump-induced scatter. (f) Extracted temperature (blue circles, right axis) and chemical potential (green circles, left axis) for the electronic distribution as a function of time, from the fits shown in (e), as well as additional intermediate times. The increase (decrease) in chemical potential for decreasing (increasing) temperature indicates the presence of an electron-like conduction band near E_F , supporting the semimetal scenario in (a). Shaded lines represent exponential decay fits. We note that due to charging effects, rigid energy offsets (relative to the Fermi edge found using a gold reference) were added in (d-e) to place the Fermi edge at E_F ; for each time trace in this figure, the same offset was applied to all $E - E_F$ vs k_x spectra.

There has been much controversy [10–14, 50, 52, 53] surrounding the subject of whether the ferromagnetic (FM) state of EuCd_2As_2 is a topological Weyl semimetal or a gapped semiconductor. Here, we present experimental evidence that the samples used in this work are semimetallic in the FM phase.

Initial work on EuCd_2As_2 described it as a Dirac semimetal above 100 K (in the paramagnetic state), and argued that at intermediate temperatures, between 100 K and the antiferromagnetic transition ($T_N = 9$ K), ferromagnetic fluctuations lead to magnetic splitting of the Dirac point into a pair of Weyl points. [13]. In this scenario, the electronic band structure of the Weyl semimetal phase includes two pairs of band crossings with linear dispersion whose nodal degeneracies lie 50 meV above the Fermi energy (E_F), as schematically depicted with blue and yellow bands in the right panel of Fig. S1a. We note that for clarity, only a single Weyl cone is schematically depicted in the right panel of Fig. S1a; the second Weyl cone is predicted to lie at the same energy but offset along the k_z direction. The hole-like band (blue), as well as the splitting thereof under ferromagnetic fluctuations, was previously measured through synchrotron ARPES studies [13]. However, because it lies above E_F , the electron-like band (yellow in Fig. S1a, right panel) could not be clearly resolved through the same measurements. Nevertheless, the dispersion of an electron-like band was faintly resolved using quasiparticle interference in scanning tunneling microscopy measurements

[14]. Further experiments stabilized FM order below a transition temperature of $T_C = 25$ K through the introduction of Eu vacancies [14]; we use the same samples as in Ref. [14] (with Eu vacancies) in this work. Hence for the samples studied in this work, we expect the presence of bulk Weyl and (potentially massive) Dirac points respectively below and above $T_C = 25$ K.

However, several recent studies instead characterize EuCd_2As_2 as a semiconductor [10–12, 53], questioning the robustness of the semimetallic characterization of EuCd_2As_2 in the earlier works. The semiconducting electronic band structure proposed in these studies is schematically depicted in the left panel of Fig. S1a, and is based on the results of Tr-ARPES [10] and La-doping-supported ARPES [11] experiments on samples grown with high-purity Eu. These measurements specifically identified a hole-like valence band with a maximum slightly above E_F (in agreement with ARPES measurements that supported the Weyl semimetal characterization), as well as a conduction band minimum 0.7–0.8 eV above E_F , but did not show evidence of an electron-like band immediately above E_F (the yellow band in the right panel of Fig. S1a). The semiconducting gap was further observed to be temperature-independent; neither the Weyl nor the Dirac semimetal phases were observed [10]. Nevertheless, we note that the existence of a large-mass conduction band 0.7 eV–0.8 eV above E_F (green band in both panels of Fig. S1a) has been confirmed by the observation of a strong peak at the corresponding infrared absorption spectrum in both samples characterized as semiconducting [10] and semimetallic [18].

Our static 6 eV laser ARPES measurements of EuCd_2As_2 , shown in Fig. S1b, corroborate equilibrium ARPES studies taken using x-ray probe photons, which unanimously report a hole-like valence band with a maximum near E_F (for both semimetallic [14] and semiconducting [10] samples). However, our time-resolved (Tr-) ARPES experiments suggest that the samples analyzed in this study are semimetallic in the FM state, by enabling the observation of semimetallic thermodynamics.

In Fig. S1c, we show the change in the spectral weight near E_F at the instant of photo-excitation with 1.2 eV photons. We observe a transient increase in electronic occupation above E_F (orange data points in Fig. S1c), accompanied by a decrease below E_F (dark blue data points in Fig. S1c). Such broadening of the Fermi edge in response to photo-excitation is ubiquitous in Tr-ARPES experiments, and is generally interpreted as rapid heating of electrons by the pump pulse, followed by the slower cooling of electrons via coupling to phonons [6]. The time trace in Fig. S1d shows electron distribution curves (EDCs) taken at various pump-probe delays for EuCd_2As_2 under 1.2 eV photo-excitation at $T \approx T_C$. At t_0 , as described earlier, there is a transient increase in population above E_F , along with a faint decrease in occupation below E_F ; these two disturbances cool over the following few picoseconds. In Fig. S1e, we demonstrate that the EDCs in Fig. S1d of hot electrons at various time delays are well-fit by Fermi-Dirac distributions multiplied by a parabolic density of states centered 50 meV above E_F . The transient electronic temperature T_e and chemical potential μ as functions of time extracted from the fits in Fig. S1e are shown in Fig. S1f. We find that the increase in electronic temperature in response to the pump pulse at $t = t_0$ is accompanied by a decrease in the extracted chemical potential. Moreover, the recovery of the electronic temperature to a quasi-equilibrium value is exponential, with a timescale (2.73 ps) approximately double that of the exponential recovery of the chemical potential (1.46 ps).

To interpret this result, we recall that the relation between the chemical potential and temperature for a (semi)metal or doped semiconductor can be derived through a Sommerfeld expansion: $\Delta\mu \propto -T^2 g'(E_F)/g(E_F)$, where $g(E)$ is the density of states in energy [54]. Crucially, this indicates that for an inherently p-doped semiconductor – in which the density of states decreases with increasing energy – an increase (decrease) in chemical potential with increasing (decreasing) temperature is expected. However, for a charge-neutral semimetal (*i.e.* a semimetal with E_F at the band crossing), the density of states increases with increasing energy, leading to an increase (decrease) in chemical potential with decreasing (increasing) temperature. We therefore assert that when the temperature of the electrons in EuCd_2As_2 is increased by the pump pulse, much of the increase in spectral weight above E_F is realized above the Weyl point in an electron-like band, which leads to the transient decrease in μ and its subsequent recovery at twice the decay rate of T . For comparison, previous Tr-ARPES experiments on strongly p-type graphene ($E_0 \approx E_F - 0.2$ eV) show simultaneous increases in both μ and T_e in response to photo-excitation [6]. We also note that similar observations have been made in the 3D Dirac semimetal Cd_3As_2 [20] and in the 2D Dirac surface states Bi_2Se_3 [55].

Finally, we note that the magnetism-induced splitting below T_C does not affect the aforementioned arguments. Due to the large expected size of the splitting (on the order of 0.1 \AA^{-1}), we expect that Fig. S1b shows the dispersion of a single Weyl fermion. The theoretical description of the dynamics shown in Fig. S1f similarly remains unchanged when we account for the presence of a second Weyl point. Moreover, across all of the experimental analysis in this study, the emergence of magnetic ordering across T_C does not significantly affect our observations, aside from shifting the plasmon energy (see the main text for further details).

Overall, though our data is consistent with the presence of a Weyl semimetal phase in the FM state, the phase diagram of EuCd_2As_2 – and the relative roles of magnetic impurities and Eu vacancies – are likely complex. EuCd_2As_2 may feature both semiconducting and semimetallic regimes, and its magnetic and (topological) electronic phase diagrams consequently merit further study.

II. TEMPERATURE-INDEPENDENCE OF THE SURFACE-STATE DISPERSION AND CIRCULAR DICHROISM ARPES MEASUREMENTS

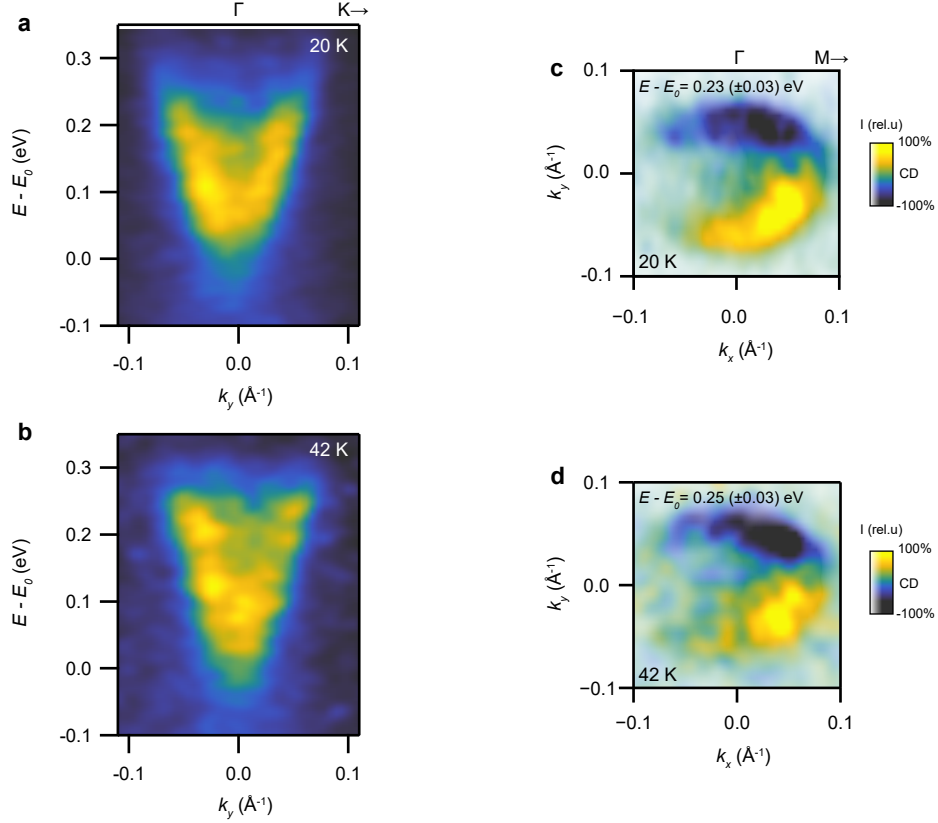


FIG. S2. **Temperature-invariance of the surface-state dispersion and circular dichroism ARPES spectra:** (a, b) ARPES spectra at t_0 in the ferromagnetic (FM) state ($T = 20$ K) and paramagnetic (PM) state ($T = 42$ K) of EuCd_2As_2 , respectively, where the PM to FM transition occurs at $T_C \approx 25$ K [14]. In (a,b), it is important to note that the conduction band below E_0 is not visible (where $E_0 \approx E_F + 0.8$ eV is the bottom of the unoccupied surface state, see Sec. III B), because the ARPES data were taken at the instant of photo-excitation, before electrons have scattered to energies significantly below those initially excited by the pump. (c, d) Constant-energy cuts of the t_0 circular dichroism ARPES (CD-ARPES) measurements at 20 K and 42 K, respectively, integrated over ± 30 meV bins around the stated center energies. Both the ARPES data in (a, b) and the CD-ARPES data in (c, d) are nearly identical above and below T_C , providing support for our focus on the PM state in our first-principles calculations (Sec. III).

To theoretically characterize the bulk and surface spectrum of EuCd_2As_2 , we performed first-principles (DFT) calculations in the paramagnetic (PM) state in Sec. III. To justify our focus on the PM state in our DFT calculations, we show in Fig. S2 ARPES (panels (a, b)) and circular dichroism ARPES (CD-ARPES, panels (c, d)) measurements of EuCd_2As_2 both below and above the ferromagnetic (FM) transition temperature of $T_C \approx 25$ K (for further characterization and details of the samples used in this study, see Ref. [14]). The data taken above and below T_C in Fig. S2 are qualitatively identical, supporting the applicability of our PM-state DFT calculations in Sec. III.

We additionally note that the PM state of EuCd_2As_2 has both inversion (\mathcal{I}) and time-reversal (\mathcal{T}) symmetry in the 3D bulk. This provides further evidence that the CD-ARPES signal in Fig. S2 corresponds to an (unoccupied) 2D surface state, because the CD-ARPES signal must vanish at all \mathbf{k} in a system with \mathcal{I} and \mathcal{T} symmetries [56].

III. FIRST-PRINCIPLES CALCULATIONS

In this section we will perform and analyze *ab initio* density-functional theory (DFT) calculations and construct Wannier tight-binding models to study the bulk electronic structure, surface states, and band topology of EuCd_2As_2 . Because the ARPES measurements in this work produced qualitatively similar data both above and below the paramagnetic (PM) to FM transition temperature of $T_c \approx 25$ K (see Fig. S5 and Sec. II), we will focus our analysis below on the simpler case of EuCd_2As_2 in the PM state. We will first in Sec. III A detail our DFT calculations and the construction of our Wannier model. In Sec. III B, we will then use surface Green's functions in a finite slab Hamiltonian to obtain the (001)- (\hat{z} -normal) surface spectrum of EuCd_2As_2 in the PM state, and quantify the contribution of the Eu $4f$ states to the surface spectrum, as they exert a strong influence on the surface chemical potential via the Hubbard U parameter in our DFT calculations (Sec. III A). Our analysis in Sec. III B reveals the presence of unoccupied (001)-surface bands that coexist with the projected continuum of unoccupied bulk states (the projected bulk conduction manifold), consistent with our Tr-ARPES experiments (see Fig. 2c of the main text).

To further our understanding of the (001)-surface states, we will next in Sec. III C compute the surface spin and orbital angular momentum (OAM) textures, which reveal the surface states to be a 2D Dirac cone with weak spin-orbit-coupling- (SOC-) driven splitting away from $\mathbf{k} = \mathbf{0}$. We will also in Sec. III C introduce a simplified low-energy $\mathbf{k} \cdot \mathbf{p}$ Hamiltonian that qualitatively reproduces the dispersion and angular momentum textures of the (001)-surface states obtained from our DFT-based calculations. Lastly, in Sec. III D, we will apply the methods of Ref. [15] to our PM-state DFT calculation to analyze the band topology of EuCd_2As_2 at and away from E_F . Through this analysis, we identify a large range of contiguous topological gaps in the bulk conduction manifold, from which we conclude that the unoccupied (001)-surface bands in EuCd_2As_2 can be viewed as the 2D topological surface states of a 3D topological band insulator phase at an electronic filling above E_F .

A. First-principles calculations and Wannier tight-binding model of the paramagnetic state of EuCd_2As_2

Site	Atom	Wyckoff Position	Atomic Position (Direct)	Wannier Center (Direct)	Wannier Orbitals (Spinful)
Eu	Eu	1a	(0.0000, 0.0000, 0.0000)	(0.0000, 0.0000, 0.0000)	$5 \times 5d + 7 \times 4f$ (total 24)
Cd ₁	Cd	2d	(0.6667, 0.3333, 0.3668)	(0.6667, 0.3333, 0.3668)	$1 \times 5s$ (total 2)
Cd ₂	Cd	2d	(0.3333, 0.6667, 0.6332)	(0.3333, 0.6667, 0.6332)	$1 \times 5s$ (total 2)
As ₁	As	2d	(0.6667, 0.3333, 0.7533)	(0.6667, 0.3333, 0.7533)	$3 \times 4p$ (total 6)
As ₂	As	2d	(0.3333, 0.6667, 0.2467)	(0.3333, 0.6667, 0.2467)	$3 \times 4p$ (total 6)

TABLE S1. **Atomic positions and Wannier centers of EuCd_2As_2 in the paramagnetic state.** In this table, we list for each atom in EuCd_2As_2 the site name, the atomic species, the site Wyckoff position, the position of the atom in direct coordinates (*i.e.* in the units of $\mathbf{a}_{1,2,3}$ in Eq. (1)), the position in direct coordinates of the Wannier orbital associated to the atom in our Wannier model, and the number and indexing of the Wannier orbitals. The atomic positions were obtained from Inorganic Crystal Structure Database (ICSD) entry number 422963 [57, 58], which we used in our DFT calculations without structural relaxation. In the Wannier model, the up- and down-spin components of each orbital lie at exactly the same positions, and the orbital centers coincide with the atomic positions to within 10^{-4} in direct coordinates. This allows us to use the Wannier model to compute the orbital angular momentum texture in Sec. III C, as further detailed below in the text surrounding Eq. (19).

To determine the bulk and surface spectrum of EuCd_2As_2 for comparison with our experimental data, we begin by performing *ab initio* calculations within the DFT framework as implemented in the **Quantum Espresso** software package [40–42]. We use as input to our calculations the atomic positions and lattice parameters in the CIF structure file for EuCd_2As_2 from Inorganic Crystal Structure Database (ICSD) entry number 422963 [57, 58], and do not perform further structural relaxation. Because the experiments in this study produced qualitatively similar data both above and below the FM transition temperature of $T_c \approx 25$ K (see Fig. S5 and Sec. II), and because the symmetry and topology of nonmagnetic 3D systems are simpler than those in magnetic phases [59, 60], then we focus our first-principles calculations on the PM state.

In the PM phase, EuCd_2As_2 respects the symmetries of nonmagnetic space group (SG) 164 ($P\bar{3}m1$). Each primitive (unit) cell of EuCd_2As_2 contains one Eu atom, two Cd atoms, and two As atoms, whose coordinates are provided in

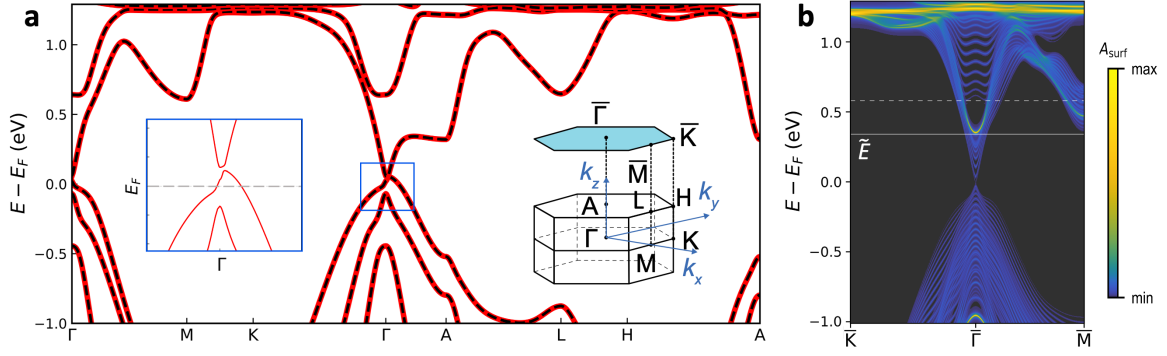


FIG. S3. **Calculated bulk band structure and surface spectral function of EuCd_2As_2 :** (a) Bulk band structure of the paramagnetic (PM) state of EuCd_2As_2 obtained from first-principles calculations (DFT, solid red lines) and the bands of a Wannier tight-binding model fit to the DFT calculation (dashed black lines, see Table S1 and the surrounding text). At intrinsic filling (ν_F in Eq. (3)), the bulk is metallic, as evidenced by the Fermi pocket at E_F in the left inset panel in (a). In (a), we also depict the bulk and (001)- (\hat{z} -normal) surface-projected Brillouin zones (BZs) for the symmetry group (SG) of the PM phase of EuCd_2As_2 , nonmagnetic SG 164 ($P\bar{3}m1$). The bands in (a) are doubly degenerate owing to the presence of bulk 3D spatial inversion (\mathcal{I}) and time-reversal (\mathcal{T}) symmetries [65, 66]. (b) The (001)-surface spectral function $A_{\text{surf}}(\mathbf{k}, E)$ (Eq. (8)) of the Wannier tight binding model. In (b), we observe a single bright surface spectral feature above E_F that lies within the projected continuum of unoccupied bulk states and exhibits an energy minimum at $\tilde{E} = E_F + 0.34 \text{ eV}$ (solid gray line). Though the surface states in (b) are quadratic at low energies, we observe that the surface bands are generally well fit by a hyperbolic dispersion with a small mass (*i.e.* a nearly linear dispersion relation). The dashed line in (b) indicates the energy at which we will shortly compute constant-energy spectral functions and spin and orbital angular momentum textures (Fig. S6).

Table S1. The primitive lattice vectors of EuCd_2As_2 are given by:

$$\begin{aligned} \mathbf{a}_1 &= (4.4499000 \text{ \AA}) \hat{\mathbf{x}}, \\ \mathbf{a}_2 &= (-2.2249500 \text{ \AA}) \hat{\mathbf{x}} + (3.8537264 \text{ \AA}) \hat{\mathbf{y}}, \\ \mathbf{a}_3 &= (7.3499999 \text{ \AA}) \hat{\mathbf{z}}. \end{aligned} \quad (1)$$

The primitive reciprocal lattice vectors of EuCd_2As_2 are then correspondingly given by:

$$\begin{aligned} \mathbf{b}_1 &= \frac{2\pi(\mathbf{a}_2 \times \mathbf{a}_3)}{\mathbf{a}_1 \cdot (\mathbf{a}_2 \times \mathbf{a}_3)} = (1.41198348 \text{ \AA}^{-1}) \hat{\mathbf{x}} + (0.81520904 \text{ \AA}^{-1}) \hat{\mathbf{y}}, \\ \mathbf{b}_2 &= \frac{2\pi(\mathbf{a}_3 \times \mathbf{a}_1)}{\mathbf{a}_1 \cdot (\mathbf{a}_2 \times \mathbf{a}_3)} = (1.63041809 \text{ \AA}^{-1}) \hat{\mathbf{y}}, \\ \mathbf{b}_3 &= \frac{2\pi(\mathbf{a}_1 \times \mathbf{a}_2)}{\mathbf{a}_1 \cdot (\mathbf{a}_2 \times \mathbf{a}_3)} = (0.85485514 \text{ \AA}^{-1}) \hat{\mathbf{z}}. \end{aligned} \quad (2)$$

In our DFT calculations, we employed the Perdew-Burke-Ernzerhof generalized gradient approximation for the exchange-correlation term [61–63] together with projected augmented-wave (PAW) pseudopotentials [64], including fully relativistic SOC in the noncollinear scheme. In this setup, when no initial magnetic moments are specified, the self-consistent cycle converges to a nonmagnetic, time-reversal- (\mathcal{T} -) invariant solution (*i.e.* a state in which the spin density vanishes at all positions in real space). Core electrons were treated by norm-conserving, optimized nonlocal pseudopotentials. The self-consistent calculations were performed over a mesh of $10 \times 10 \times 5$ \mathbf{k} points. The kinetic energy cutoff was set to 680 eV. To properly localize the half-filled Eu $4f$ orbitals in the PM state, correct self-interaction errors, and to improve the overall accuracy of the PM-state band structure, a Hubbard U correction of $U = 5$ eV on the Eu sites was implemented within the GGA + U scheme [43].

The resulting band structure is plotted in Fig. S3a with solid red lines. Each of the bands in Fig. S3a is doubly degenerate due to the presence of bulk 3D spatial inversion (\mathcal{I}) and \mathcal{T} symmetries [65, 66]. At intrinsic filling, EuCd_2As_2 carries an odd number of valence electrons ν_F per unit cell:

$$\nu_F = 51. \quad (3)$$

Because $\nu_F \bmod 2 = 1$, then due to \mathcal{T} symmetry in the PM state, EuCd_2As_2 is a filling-enforced metal at E_F (indicated by the red dashed line in the left inset in Fig. S3a) [66, 67]. Just above E_F , at a filling of $\nu_F + 1$, there is

instead an energy gap, and the system can be viewed overall as a weakly massive 3D Dirac semimetal. We will shortly below in Sec. III D show that the gap at $\nu_F + 1$ is topological, and more generally analyze the system topology at and away from E_F .

Our choice of $U = 5$ eV and the accuracy of the DFT band structure in Fig. S3a are supported by previous theoretical and experimental studies of EuCd_2As_2 . First, previous DFT calculations performed with $U = 5$ eV in the FM state were found to accurately reproduce the ARPES spectrum of the occupied bands, importantly including the energies of the Eu $4f$ orbitals, over a wide energy range [14, 52]. DFT + U calculations with $U = 5$ eV in the PM state were also found to accurately capture the ARPES spectrum in the PM phase [13], and closely match the band structure in Fig. S3a over the energy range $E_F \pm 1$ eV. Lastly, recent ARPES measurements of the *unoccupied* band structure have determined the first large energy gap above E_F near Γ to be approximately ~ 0.7 eV in the PM state [10, 11], consistent with the DFT band structure in Fig. S3a (specifically the gap between the doubly degenerate conduction bands in the left inset and the next lowest doubly degenerate conduction bands at Γ , which are nondispersing to leading order).

To analyze the spectrum and topology of the PM state, we next employ Wannier functions [44–46] to construct a tight-binding model of EuCd_2As_2 , constrained to closely reproduce the energy spectrum obtained from DFT within a few eV of E_F (black dashed lines in Fig. S3a). We specifically construct our Wannier model using the Eu $5d$ and $4f$, Cd $5s$, and As $4p$ orbitals with SOC ($N_a = 20$ spin-degenerate pairs of orbitals). We then symmetrize the Wannier model [47] using the crystal symmetries in SG 164 ($P\bar{3}m1$) and \mathcal{T} . The locations of the resulting Wannier centers are provided in Table S1, and coincide with the atomic positions to within 10^{-4} in the units of $\mathbf{a}_{1,2,3}$ in Eq. (1).

B. Surface spectral function calculation details

We will next use the Wannier-based tight-binding Hamiltonian for the PM phase of EuCd_2As_2 previously obtained from DFT calculations in Sec. III A to compute the (001)-surface states. We begin by cutting the Wannier model into a slab geometry that is finite in the z -direction while retaining periodicity in the (x, y) -plane, resulting in a slab Hamiltonian H_{slab} . We then partially Fourier transform H_{slab} to obtain the slab Bloch Hamiltonian $H_{\text{slab}}(\mathbf{k})$, where \mathbf{k} denotes a vector in the space of the in-plane crystal momenta:

$$\mathbf{k} \equiv (k_1, k_2), \quad (4)$$

where $k_{1,2}$ respectively lie along the reciprocal lattice vectors $\mathbf{b}_{1,2}$ in Eq. (2). The slab Bloch Hamiltonian $H_{\text{slab}}(\mathbf{k})$ is consequently a square matrix of dimension:

$$N = N_s \times N_a \times N_L, \quad (5)$$

where $N_s = 2$ is the number of spin components, $N_a = 20$ is the number of (Kramers pairs of) orbitals per layer (slab unit cell), and N_L is the number of layers. Throughout all of the slab-based calculations in this work, we fix $N_L = 40$.

We next define the retarded Green's function at a given energy E and in-plane momentum \mathbf{k} to be:

$$G^R(\mathbf{k}, E) = ((E - E_F)\mathbb{1}_{N \times N} - H_{\text{slab}}(\mathbf{k}) + i\Omega\mathbb{1}_{N \times N})^{-1}, \quad (6)$$

where $\mathbb{1}_{N \times N}$ is the $N \times N$ identity matrix and Ω is a phenomenological broadening parameter. For all of the theoretical spectral function calculations in this work, we choose $\Omega = 3.87$ meV such that Ω is equal to $k_B T$ for $T = 45$ K, which lies just above the temperature range in which our PM-state ARPES measurements were performed (see for example Sec. II). To restrict consideration to spectral weight on the top slab surface, we then construct the top-surface projector:

$$P_t = \sum_{s=\uparrow, \downarrow} \sum_{a=1}^{N_a} |\psi_{s,a,N_L}\rangle \langle \psi_{s,a,N_L}|, \quad (7)$$

where $|\psi_{s,a,i}\rangle$ is a tight-binding (Wannier) basis state of the slab model with a spin index s , an orbital index a , and a layer (slab unit cell) index i (see the text surrounding Eq. (5)). In Eq. (7), P_t is hence an $N \times N$ matrix. In the basis of the underlying spins, orbitals, and layers, P_t is a diagonal matrix whose elements are equal to 1 for basis states belonging to the top layer, and are 0 for all other basis states. Lastly, we define the *top-surface spectral function* $A_{\text{surf}}(\mathbf{k}, E)$ at each \mathbf{k} and E by taking the imaginary part of the trace of $G^R(\mathbf{k}, E)$ in Eq. (6) projected to the top surface [68, 69]:

$$A_{\text{surf}}(\mathbf{k}, E) = -\frac{1}{\pi} \text{Im Tr}[P_t G^R(\mathbf{k}, E) P_t] = -\frac{1}{\pi} \text{Im Tr}[P_t G^R(\mathbf{k}, E)], \quad (8)$$

in which we have simplified using the projector idempotence $P_t^2 = P_t$ and the cyclic property of the trace.

To make contact between $A_{\text{surf}}(\mathbf{k}, E)$ and the full density of states, we first examine the full spectral function $A(\mathbf{k}, E)$ realized by neglecting (setting to identity) the factor of P_t in Eq. (8). We begin this analysis by considering the action of $G^R(\mathbf{k}, E)$ on a Bloch eigenstate $|n\mathbf{k}\rangle$, for which:

$$H_{\text{slab}}(\mathbf{k})|n\mathbf{k}\rangle = E_n(\mathbf{k})|n\mathbf{k}\rangle. \quad (9)$$

Because $[H_{\text{slab}}(\mathbf{k}), G^R(\mathbf{k}, E)] = 0$, then Eqs. (6) and (9) imply that:

$$G^R(\mathbf{k}, E)|n\mathbf{k}\rangle = \left(\frac{1}{(E - E_F) - E_n(\mathbf{k}) + i\Omega} \right) |n\mathbf{k}\rangle, \quad (10)$$

such that $G^R(\mathbf{k}, E)$ can be re-expressed through the spectral decomposition:

$$G^R(\mathbf{k}, E) = \sum_{n=1}^N \frac{|n\mathbf{k}\rangle\langle n\mathbf{k}|}{(E - E_F) - E_n(\mathbf{k}) + i\Omega}. \quad (11)$$

Inserting Eq. (11) into Eq. (8) with P_t set to the identity then returns a spectral function $A(\mathbf{k}, E)$ for the entire slab at each \mathbf{k} :

$$\begin{aligned} A(\mathbf{k}, E) &= -\frac{1}{\pi} \text{Im Tr}[G^R(\mathbf{k}, E)] \\ &= -\sum_{n=1}^N \frac{1}{\pi} \text{Im} \frac{1}{(E - E_F) - E_n(\mathbf{k}) + i\Omega} \\ &= \sum_{n=1}^N \frac{1}{\pi} \frac{\Omega}{[E - E_F - E_n(\mathbf{k})]^2 + \Omega^2} \\ &\equiv \sum_{n=1}^N \delta_{\Omega}(E - E_F - E_n(\mathbf{k})), \end{aligned} \quad (12)$$

where in the final line, we recognize the preceding expression as the Lorentzian representation of the Dirac delta function $\delta_{\Omega}(E - E_F - E_n(\mathbf{k}))$. The overall spectral function $A(\mathbf{k}, E)$ in Eq. (12) hence characterizes the Fourier-transformed density of states [69–71]. Due to the strongly nonlinear (delta-function-like) profile of $A(\mathbf{k}, E)$ in Eq. (12), we therefore throughout this work plot all spectral functions on a logarithmic scale with arbitrary units (a.u.).

Next, to understand the role of P_t in Eq. (8), we simplify the trace in Eq. (8) by combining Eqs. (7) and (11):

$$\text{Tr}[P_t G^R(\mathbf{k}, E)] = \sum_n \frac{\langle n\mathbf{k}|P_t|n\mathbf{k}\rangle}{(E - E_F) - E_n(\mathbf{k}) + i\Omega} = \sum_{s=\uparrow,\downarrow} \sum_{a=1}^{N_a} \sum_{n=1}^N \frac{|\langle \psi_{s,a,N_L} | n\mathbf{k} \rangle|^2}{(E - E_F) - E_n(\mathbf{k}) + i\Omega}. \quad (13)$$

Because each overlap magnitude $|\langle \psi_{s,a,N_L} | n\mathbf{k} \rangle|^2$ in Eq. (13) is real, then using Eq. (12), the surface spectral function $A_{\text{surf}}(\mathbf{k}, E)$ in Eq. (8) becomes:

$$\begin{aligned} A_{\text{surf}}(\mathbf{k}, E) &= \sum_{s=\uparrow,\downarrow} \sum_{a=1}^{N_a} \sum_{n=1}^N |\langle \psi_{s,a,N_L} | n\mathbf{k} \rangle|^2 \left[-\frac{1}{\pi} \text{Im} \frac{1}{(E - E_F) - E_n(\mathbf{k}) + i\Omega} \right] \\ &= \sum_{s=\uparrow,\downarrow} \sum_{a=1}^{N_a} \sum_{n=1}^N |\langle \psi_{s,a,N_L} | n\mathbf{k} \rangle|^2 \delta_{\Omega}(E - E_F - E_n(\mathbf{k})). \end{aligned} \quad (14)$$

Overall, the form of Eq. (14) indicates that $A_{\text{surf}}(\mathbf{k}, E)$ is similar in structure to the total spectral function $A(\mathbf{k}, E)$ in Eq. (12), but instead measures the weight of each slab Bloch eigenstate $|n\mathbf{k}\rangle$ at $E - E_F$ on the top surface via the combination of $\delta_{\Omega}(E - E_F - E_n(\mathbf{k}))$ and the overlap magnitudes of $|n\mathbf{k}\rangle$ with the top-surface basis states. In Fig. S3b, we show the (001)-surface spectral function of the PM state of EuCd_2As_2 computed using Eq. (8). The surface spectrum consists of a single hyperbolic feature that lies within the continuum of unoccupied bulk states (the projected bulk conduction manifold).

Before analyzing the angular momentum textures and topological origin of the unoccupied (001)-surface states in Fig. S3b (which will shortly be done in Secs. III C and III D), we will establish the degree to which the chemical

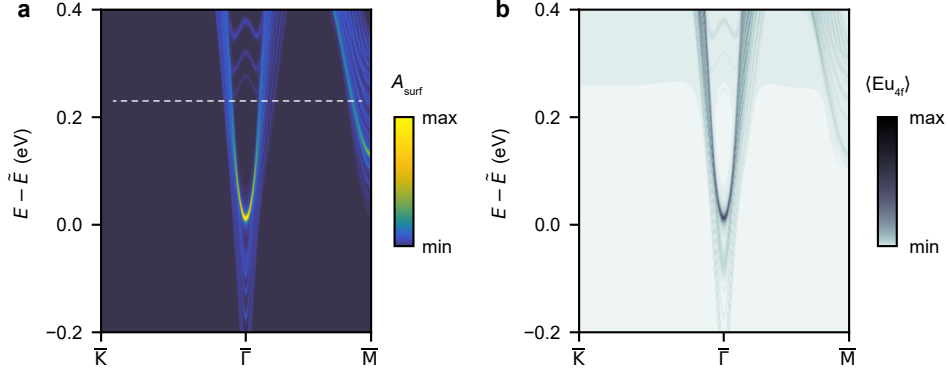


FIG. S4. **Weight of the Eu 4f states in the (001)-surface spectral function:** (a) The (001)-surface spectral function $A_{\text{surf}}(\mathbf{k}, E)$ (Eq. (8)) reproduced from Fig. S3b and plotted relative to the minimum energy of the unoccupied surface states \tilde{E} . (b) The projected weight of the Eu 4f orbitals $\langle \text{Eu}_{4f}(\mathbf{k}, E) \rangle$ in the (001)-surface states (Eq. (16)). Taken together, the data in (a,b) indicate that the unoccupied surface states carry a very large contribution from the Eu 4f orbitals, whose bulk chemical potential is set by the value of the Hubbard correction $U = 5$ eV in our DFT calculations (see the text surrounding Eq. (3)).

potential of the surface states $\tilde{E} = E_F + 0.34$ eV depends on our bulk calculation details. This information is especially important because the unoccupied surface states in our ARPES measurements appear at relatively higher energies, specifically instead exhibiting a band minimum at $E_0 \approx E_F + 0.8$ eV as estimated from the kinetic energy of photoelectrons. First, \tilde{E} depends on the choice of surface termination atoms in our slab model, an effect that itself is typically significant in models of the surface states of real solid-state materials [72–74]. Furthermore, in our EuCd_2As_2 samples, we do not have atomistic knowledge of the (001)-surface probed in our ARPES experiments with which to calibrate the slab surface termination in our DFT- and Wannier-based surface-state calculations. Next, \tilde{E} in Fig. S3b is also dependent on the value of U employed in our bulk DFT + SOC + U calculations (Sec. III A). Specifically, in modeling the PM state of EuCd_2As_2 , we have incorporated a large Coulomb term $U = 5$ eV in our DFT + SOC + U calculations to shift the half-filled, nearly-flat Eu 4f states away from E_F . The choice of U in turn influences the surface-state chemical potential \tilde{E} via the spectral weight of the Eu 4f orbitals in the surface bands.

We therefore next quantify the contribution of Eu 4f states to the surface spectrum. To accomplish this, we first construct a projector P_{4f} onto the Eu 4f states in the slab model:

$$P_{4f} = \sum_{s=\uparrow,\downarrow} \sum_{a \in \{\text{Eu}_{4f}\}} \sum_{i=1}^{N_L} |\psi_{s,a,i}\rangle \langle \psi_{s,a,i}|, \quad (15)$$

where $|\psi_{s,a,i}\rangle$ and N_L are defined in the text surrounding Eq. (7). Similar to P_t in Eq. (7), when P_{4f} is placed in the basis of the spins, orbitals, and layers of the slab model, P_{4f} is a diagonal matrix whose elements are equal to 1 for basis states belonging to the Eu 4f orbital subspace, and are 0 for all other basis states. Using Eqs. (6), (7), and (15), we then define a spectral function $\langle \text{Eu}_{4f}(\mathbf{k}, E) \rangle$ that is only large for the subset of the surface spectral weight that derives from the Eu 4f orbitals:

$$\langle \text{Eu}_{4f}(\mathbf{k}, E) \rangle = -\frac{1}{\pi} \text{Im Tr} [P_{4f} P_t G^R(\mathbf{k}, E) P_t]. \quad (16)$$

In Fig. S4b, we plot $\langle \text{Eu}_{4f}(\mathbf{k}, E) \rangle$ for the (001)-surface of EuCd_2As_2 . Comparing $\langle \text{Eu}_{4f}(\mathbf{k}, E) \rangle$ in Fig. S4b to the overall surface spectral function $A_{\text{surf}}(\mathbf{k}, E)$ in Fig. S4a, we find that the hyperbolic surface state at \tilde{E} carries a very large contribution from the Eu 4f states. This implies that beyond surface termination effects, \tilde{E} is highly dependent on the value of U employed in our DFT + SOC + U calculations (which was chosen to match previous bulk DFT calculations and ARPES measurements, see the text following Eq. (3)).

Hence, \tilde{E} in our theoretical calculations can be directly tuned by varying the slab surface chemical potential and the bulk value of U . However, the dispersion relation and matrix elements of the (001)-surface states derive in a more complicated manner from the bulk band structure (and topology, see Sec. III D). Furthermore, as discussed in the text following Eq. (3), the *bulk* band structure of the Wannier model (dashed black lines in Fig. S3a) shows close agreement with previous studies of EuCd_2As_2 [10, 11, 13, 14, 52]. Together, this suggests the possibility that we may interpret the shift in \tilde{E} relative to its experimental value E_0 as a leading order correction, and more simply treat the

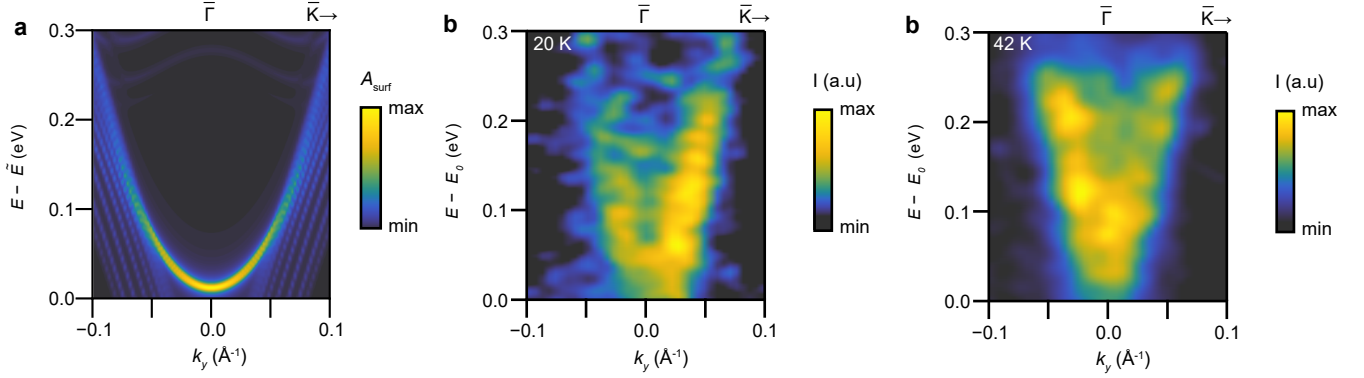


FIG. S5. **Comparison between the DFT-obtained surface spectral function and the unoccupied surface-state dispersion in Tr-ARPES measurements:** (a) The (001)-surface spectral function $A_{\text{surf}}(\mathbf{k}, E)$ (Eq. (8)) of the Wannier-based slab model obtained from our DFT calculations (Fig. S3b), plotted relative to the minimum energy of the surface states \tilde{E} along k_y ($\bar{\Gamma} - \bar{K}$ in the surface BZ in Fig. S3a), and zoomed into the momentum range accessible in our Tr-ARPES experiments. (b, c) ARPES spectra of the unoccupied band structure plotted relative to the minimum energy of the surface states E_0 along $\bar{\Gamma} - \bar{K}$ in the surface BZ, respectively taken below ($T = 20$ K) and above ($T = 42$ K) the PM to FM transition temperature $T_C \approx 25$ K. The ARPES data in (b) were obtained by integrating over a small window after photo-excitation ($t - t_0 \in [0 \text{ ps}, 2 \text{ ps}]$), whereas the spectrum in (c) was measured at $t = t_0$ and generated by summing spectra acquired with left- and right-circularly polarized probes (further circular dichroism measurements are provided in Sec. II). The experimental dispersions relative to E_0 in (b,c) show strong qualitative agreement with the DFT-obtained (001)-surface states viewed relative to \tilde{E} in (a).

DFT-obtained (001)-surface states at \tilde{E} in Figs. S3b and S4a as representative of the physical unoccupied surface states in our ARPES experiments shifted by a *surface* chemical potential.

To support this interpretation, in Fig. S5, we plot the DFT-obtained surface spectrum as a function of k_y and $E - \tilde{E}$ compared to ARPES measurements of the (001)-surface states as functions of k_y and $E - E_0$ both above and below the PM to FM transition temperature $T_C \approx 25$ K. Though the ARPES measurements show a hyperbolic surface state with a slightly higher velocity, the theoretical dispersion relation in Fig. S5a and the experimental (001)-surface-state dispersions both above (Fig. S5c) and below (Fig. S5b) T_C show close qualitative agreement. Even stronger support for our theoretical treatment of the (001)-surface states can be obtained by comparing the circular dichroism (CD-) ARPES data to the OAM texture at the same energy 0.23 eV relative to the minimum of the surface band. Specifically, as highlighted in Fig. 2d,e of the main text, the $\langle L_{xz} \rangle = \langle \frac{L_x + L_z}{\sqrt{2}} \rangle$ component of the OAM-dependent spectral function vector in the Wannier-based model (Eq. (19) and Fig. S6c) at $\tilde{E} + 0.23$ eV (the dashed lines in Figs. S3b and S4a) shows excellent agreement with CD-ARPES measurements taken both above and below T_C at approximately 0.23 eV above E_0 (Fig. S2c,d).

C. Spin and orbital textures of the (001)-surface states

To better understand the properties of the unoccupied surface bands in Fig. S3b, and to draw connection with our circular dichroism (CD-) ARPES experiments (Sec. II), we will next extract the spin and OAM textures of the (001)-surface states. We will then introduce and analyze a simple $\mathbf{k} \cdot \mathbf{p}$ model that reproduces the dispersion and angular momentum textures of the surface conduction bands in EuCd_2As_2 .

First, to compute the spin texture, we introduce the surface-projected, spin-dependent spectral function vector $\langle \mathbf{S}(\mathbf{k}, E) \rangle$, whose components are given by [69, 75–77]:

$$\langle S_\alpha(\mathbf{k}, E) \rangle = -\frac{1}{\pi} \text{Im Tr} [\hat{S}_\alpha P_t G^R(\mathbf{k}, E) P_t], \quad (17)$$

where $G^R(\mathbf{k}, E)$ and P_t are respectively defined in Eqs. (6) and (7), and where \hat{S}_α is the α -th component of the spin operator vector $\hat{\mathbf{S}} = (\hat{S}_x, \hat{S}_y, \hat{S}_z)$. In the basis of the spins and orbitals in the slab Wannier model of EuCd_2As_2 constructed in Secs. III A and III B, and in reduced units in which the spin eigenvalues are ± 1 , the spin operator

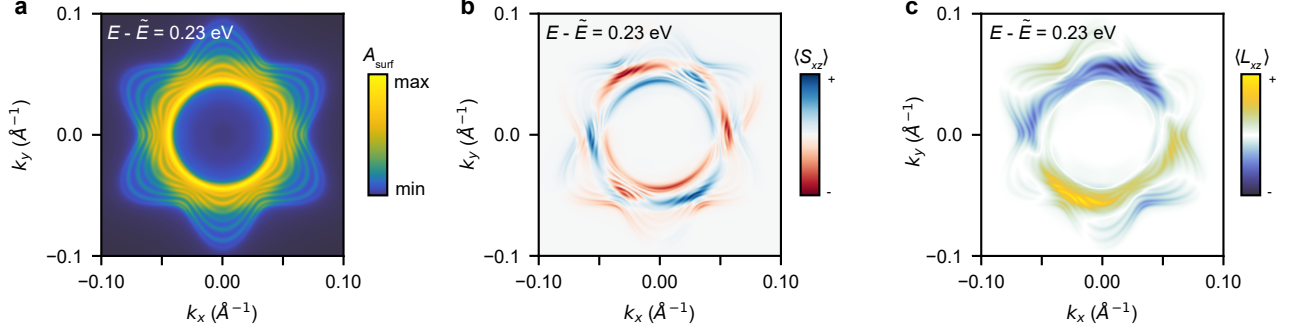


FIG. S6. **Constant-energy surface spectrum and spin and orbital angular momentum textures in the Wannier-based model:** (a) The (001)-surface spectral function $A_{\text{surf}}(\mathbf{k}, E)$ (Eq. (8)) of the Wannier-based slab model obtained from our DFT calculations of the electronic structure of EuCd_2As_2 in the PM state (Fig. S3a), plotted at a constant energy 0.23 eV (the dashed line in Figs. S3b and S4a) above the minimum energy of the surface band \tilde{E} (the solid gray line in Fig. S3b). The value of $E - \tilde{E} = 0.23$ eV was chosen to match our constant-energy (CD-) ARPES measurements, which were taken approximately 0.23 eV above the experimentally observed surface band minimum E_0 (see Sec. II and the text following Eq. (16)). The total spectral function $A_{\text{surf}}(\mathbf{k}, E)$ in (a) is dominated by a nearly circular feature surrounding $\mathbf{k} = \mathbf{0}$ with weaker hexagonal corrections. (b) The $\langle S_{xz} \rangle = \langle \frac{S_x + S_z}{\sqrt{2}} \rangle$ component of the surface spin texture vector $\langle \mathbf{S}(\mathbf{k}, E) \rangle$ (Eq. (17)), plotted at the same constant energy as $A_{\text{surf}}(\mathbf{k}, E)$ in (a). $\langle S_{xz}(\mathbf{k}, E) \rangle$ in (b) exhibits two concentric rings with alternately signed $\langle S_{xz} \rangle$ spin polarizations, revealing that the circular surface spectral feature in (a) consists of two narrowly split surface Fermi pockets that together originate from a 2D surface Dirac cone at $\mathbf{k} = \mathbf{0}$ with extremely weak spin-orbit-coupling- (SOC-) driven splitting. (c) The $\langle L_{xz} \rangle = \langle \frac{L_x + L_z}{\sqrt{2}} \rangle$ component of the surface orbital angular momentum (OAM) texture vector $\langle \mathbf{L}(\mathbf{k}, E) \rangle$ (Eq. (19)), plotted at the same constant energy as the spectra in (a,b). We selected $\langle L_{xz} \rangle$ in (c) to align with our experimental CD-ARPES measurement geometry (see the text following Eq. (38), Fig. 2b,d of the main text, and the Methods section). Unlike $\langle S_{xz}(\mathbf{k}, E) \rangle$ in (b), $\langle L_{xz}(\mathbf{k}, E) \rangle$ in (c) exhibits the same sign on each ring-like Fermi pocket of the surface Dirac cone. Overall, the OAM texture in (c) shows excellent agreement with our CD-ARPES measurements, both above and below the PM to FM transition temperature $T_C \approx 25$ K (see Fig. S2c,d and the text following Eq. (16)).

components \hat{S}_α are represented as $N_a N_L N_s \times N_a N_L N_s = N \times N$ matrices S_α :

$$S_\alpha = \mathbb{1}_{N_a N_L \times N_a N_L} \sigma_\alpha, \quad \alpha = x, y, z, \quad (18)$$

where $\sigma_{x,y,z}$ are 2×2 Pauli matrices that act in the spin subspace, $\mathbb{1}_{N_a N_L \times N_a N_L}$ is the $N_a N_L \times N_a N_L$ identity matrix, and where $N_a = 20$ and $N_L = 40$ are respectively the number of Kramers pairs of orbitals in each unit cell of the bulk Wannier model and the number of layers in the slab Hamiltonian (Eq. (5)). In order to ensure that the representation S_α of \hat{S}_α is \mathbf{k} -independent in the tight-binding (periodic) gauge of $H_{\text{slab}}(\mathbf{k})$ (Eq. (9)) in which physical and topological quantities are correctly embedded [78–80], we have constructed the Wannier model in a manner in which the up- and down-spin components of each Wannier orbital in Table S1 occupy the same positions in real space. Because $\langle \mathbf{S}(\mathbf{k}, E) \rangle$ is odd under \mathcal{T} and even under \mathcal{I} (*i.e.* transforms as a \mathcal{T} -odd axial vector), $\langle \mathbf{S}(\mathbf{k}, E) \rangle$ must vanish in bulk systems with \mathcal{I} and \mathcal{T} symmetry. However, on the 2D surfaces of 3D systems, which cannot carry \mathcal{I} as a symmetry [66], $\langle \mathbf{S}(\mathbf{k}, E) \rangle$ can be nonvanishing. Like the surface spectral function $A_{\text{surf}}(\mathbf{k}, E)$ in Eq. (8), we throughout this work plot $\langle S_\alpha(\mathbf{k}, E) \rangle$ on a log scale with arbitrary units (a.u.), but now allow for signed data represented using a color map in which blue is positive and red is negative.

To provide context for the spin texture, we first in Fig. S6a plot a constant-energy cut of the total (001)-surface spectral function $A_{\text{surf}}(\mathbf{k}, E)$ (Eq. (8)) taken 0.23 eV above the surface-state minimum \tilde{E} (the dashed line in Figs. S3b and S4a), which approximately corresponds to the same energy offset from the experimental surface-state band minimum E_0 as our constant-energy ARPES measurements (see Sec. II and the text following Eq. (16)). The total surface spectral function in Fig. S6a is dominated by a nearly circular feature surrounding $\mathbf{k} = \mathbf{0}$ with weaker hexagonal corrections. We then in Fig. S6b plot the $\langle S_{xz} \rangle = \langle \frac{S_x + S_z}{\sqrt{2}} \rangle$ component of the spin-dependent spectral function $\langle \mathbf{S}(\mathbf{k}, E) \rangle$ (Eq. (17)) at the same constant energy as $A_{\text{surf}}(\mathbf{k}, E)$ in Fig. S6a, where we have selected the $\langle S_{xz} \rangle$ component to match the alignment of our experimental CD-ARPES probe of the OAM texture (further detailed below in the text following Eq. (38)). Surprisingly, $\langle S_{xz}(\mathbf{k}, E) \rangle$ in Fig. S6b consists of two concentric rings with alternately signed $\langle S_{xz} \rangle$ spin polarizations. This indicates that the circular surface spectral feature in Fig. S6a is in fact not one surface Fermi pocket, but is rather *two* narrowly split Fermi pockets that together originate from a 2D surface Dirac cone with extremely weak SOC splitting. As we will discuss below in Sec. III D, the (001)-surface Dirac cone at $\mathbf{k} = \mathbf{0}$

in our Wannier-based calculations of EuCd_2As_2 can more specifically be viewed as the 2D topological surface state of a 3D topological band insulator phase [81, 82] at an electronic filling above the Fermi level $\nu > \nu_F$ (Eq. (3)), which can be accessed by photo-doping experiments like those in the present study.

We next turn our attention to the orbital texture of the (001)-surface states, which is closely linked to our CD-ARPES experiments. Specifically, of the different \mathbf{k} -resolved contributions to the orbital magnetization, CD-ARPES most directly couples to the local (in real space) contribution to the OAM from the underlying atomic orbitals [83–86]. To probe the atomic-orbital contribution to the OAM, we construct a surface-projected, OAM-dependent spectral function vector $\langle \mathbf{L}(\mathbf{k}, E) \rangle$, analogous to the surface-projected, spin-dependent spectral function vector $\langle \mathbf{S}(\mathbf{k}, E) \rangle$ in Eq. (17), whose components are given by [56, 77]:

$$\langle L_\alpha(\mathbf{k}, E) \rangle = -\frac{1}{\pi} \text{Im Tr} [\hat{L}_\alpha P_t G^R(\mathbf{k}, E) P_t], \quad (19)$$

where $G^R(\mathbf{k}, E)$ and P_t are respectively defined in Eqs. (6) and (7), and where \hat{L}_α is the α -th component of the OAM operator vector $\hat{\mathbf{L}} = (\hat{L}_x, \hat{L}_y, \hat{L}_z)$. Like $\langle \mathbf{S}(\mathbf{k}, E) \rangle$ in Eq. (17), $\langle \mathbf{L}(\mathbf{k}, E) \rangle$ transforms as a \mathcal{T} -odd axial vector, and must hence vanish at each \mathbf{k} in bulk systems with \mathcal{I} and \mathcal{T} symmetry. However, on the 2D surfaces of 3D systems, $\langle \mathbf{L}(\mathbf{k}, E) \rangle$ can similarly be nonvanishing due to the absence of 3D \mathcal{I} (or $\mathcal{I} \times \mathcal{T}$) symmetry.

Unlike the spin operator components \hat{S}_α , the OAM operator components \hat{L}_α have more complicated representations in the Wannier basis, and are also more sensitive to the numerical Wannierization procedure. Specifically, in order to interpret $\langle L_\alpha(\mathbf{k}, E) \rangle$ as a physical observable, it is crucial that the value of $\langle L_\alpha(\mathbf{k}, E) \rangle$ at each \mathbf{k} does not depend on the arbitrary piece of the gauge of the wavefunctions $|n\mathbf{k}\rangle$ (Eq. (9)) of the slab Bloch Hamiltonian $H_{\text{slab}}(\mathbf{k})$ (*i.e.* the free gauge factors that do not affect the real-space model embedding [78–80]). This can most straightforwardly be accomplished by requiring that, like S_α in Eq. (18), each OAM operator component \hat{L}_α is represented as a \mathbf{k} -independent matrix L_α in the tight-binding (periodic) gauge of $H_{\text{slab}}(\mathbf{k})$. In turn, in order for the matrix representatives L_α of \hat{L}_α to be \mathbf{k} -independent, each of the Wannier orbitals associated to the same atomic shell of each atom – specifically the Wannier orbitals for each atom that are assigned the same principal (n) and azimuthal (ℓ , *i.e.* OAM) quantum numbers – must occupy the same positions in real space. This ensures that each OAM operator component \hat{L}_α acts locally on the real-space tight-binding basis states, such that the basis-state positions remain invariant under the action of \hat{L}_α for all α . In the Wannier tight-binding model that we constructed for the PM state of EuCd_2As_2 in Sec. III A, the basis-state positions (Table S1) not only satisfy the above requirement, but are even more tightly grouped. Specifically, as shown in Table S1, each of the Wannier orbitals in our model coincides with the position of its associated atom to within 10^{-4} in the units of the lattice vectors $\mathbf{a}_{1,2,3}$ in Eq. (1). Our Wannier model is hence suitably constructed for computing the surface-state OAM texture $\langle \mathbf{L}(\mathbf{k}, E) \rangle$ in Eq. (19).

Having established that the surface OAM texture $\langle \mathbf{L}(\mathbf{k}, E) \rangle$ can be computed by applying Eq. (19) to our Wannier tight-binding model, we next turn our attention to constructing the OAM matrix representatives L_α in the Wannier basis. In reduced units in which $\hbar = 1$, the OAM operator components \hat{L}_α are specifically represented in the slab Wannier model constructed in Sec. III B as $N_a N_L N_s \times N_a N_L N_s = N \times N$ matrices L_α that each take a block form:

$$L_\alpha = \left\{ \bigoplus_{\xi, \ell_\xi \neq 0} L_\alpha^{\xi, \ell_\xi} \right\} \oplus \left\{ \bigoplus_{\xi, \ell_\xi = 0} \mathbb{0}_{N_s N_L \times N_s N_L} \right\}, \quad (20)$$

where each L_α^{ξ, ℓ_ξ} is proportional to the identity in the $N_s N_L \times N_s N_L = 2N_L \times 2N_L$ spin and layer subspace (Eq. (5)), and where $\mathbb{0}_{N_s N_L \times N_s N_L}$ is the $N_s N_L \times N_s N_L$ matrix of zeroes. In Eq. (20), ξ and ℓ_ξ respectively run in Table S1 over the “Site” column and the OAM quantum numbers ℓ_ξ per site in the “Wannier Orbitals” column, such that for example the $\ell = 2$ d and $\ell = 3$ f orbitals of the $1a$ Eu atom are included in the first direct sum ($\ell_\xi \neq 0$) and excluded in the second ($\ell_\xi = 0$), whereas for example the $\ell = 0$ s orbitals of the $2d$ Cd atoms are excluded from the first direct sum and included in the second. Each L_α^{ξ, ℓ_ξ} in Eq. (20) is hence an $N_L N_s (2\ell_\xi + 1) \times N_L N_s (2\ell_\xi + 1)$ matrix [87].

To obtain the matrices L_α^{ξ, ℓ_ξ} in Eq. (20) in the Wannier tight-binding basis, we first recognize that each atomic orbital in our model is expressed in the real cubic-harmonic basis [88]:

$$\{s, p_x, p_y, p_z, d_{z^2}, d_{xz}, d_{yz}, d_{x^2-y^2}, d_{xy}, \dots\}, \quad (21)$$

rather than in the complex spherical-harmonic basis $\{Y_\ell^m\}$ in which L_z^{ξ, ℓ_ξ} is a diagonal matrix whose only nonzero elements take values given by the orbital magnetic quantum numbers m [87, 89]. Our strategy for constructing each $L_{x,y,z}^{\xi, \ell_\xi}$ matrix therefore consists of two steps: (i) we first construct $L_{x,y,z}^{\xi, \ell_\xi}$ in the familiar basis of spherical harmonics, and (ii) we then apply a unitary transformation to rotate $L_{x,y,z}^{\xi, \ell_\xi}$ into the cubic-harmonic Wannier basis.

We next recognize that given an OAM matrix representative $(L_z^{\xi, \ell_\xi})^{(\ell)}$ in the spherical-harmonic basis (denoted by the superscript (ℓ) here and below) with the eigenstates $|\ell, m\rangle$ such that:

$$(L_z^{\xi, \ell_\xi})^{(\ell)} |\ell, m\rangle = m |\ell, m\rangle, \quad (22)$$

there exist ladder operators $\hat{L}_\pm^{\xi, \ell_\xi}$ that change m by one unit within the ℓ_ξ manifold [90]:

$$\hat{L}_\pm^{\xi, \ell_\xi} |\ell, m\rangle = \sqrt{\ell_\xi(\ell_\xi + 1) - m(m \pm 1)} |\ell, m \pm 1\rangle. \quad (23)$$

Using Eq. (23), we then construct the matrix representatives $(L_\pm^{\xi, \ell_\xi})^{(\ell)}$ of $\hat{L}_\pm^{\xi, \ell_\xi}$, whose matrix elements are given by:

$$\left[(L_\pm^{\xi, \ell_\xi})^{(\ell)} \right]_{m, m'} = \sqrt{\ell_\xi(\ell_\xi + 1) - m'(m' \pm 1)} \delta_{m, m' \pm 1}. \quad (24)$$

The $\alpha = x, y, z$ OAM matrix representatives in the spherical-harmonic basis are then by definition given by [87, 90]:

$$(L_x^{\xi, \ell_\xi})^{(\ell)} = \frac{1}{2} \left\{ (L_+^{\xi, \ell_\xi})^{(\ell)} + (L_-^{\xi, \ell_\xi})^{(\ell)} \right\}, \quad (L_y^{\xi, \ell_\xi})^{(\ell)} = \frac{1}{2i} \left\{ (L_+^{\xi, \ell_\xi})^{(\ell)} - (L_-^{\xi, \ell_\xi})^{(\ell)} \right\}. \quad (25)$$

Lastly, each cubic-harmonic (Wannier-basis) eigenstate $|\ell, \mu\rangle_{\text{cub}}$ represents a linear combination of the spherical-harmonic eigenstates $|\ell, m\rangle$ [88]:

$$|\ell, \mu\rangle_{\text{cub}} = \sum_{m=-\ell}^{+\ell} [U^\ell]_{\mu m} |\ell, m\rangle. \quad (26)$$

Using Eq. (26), we hence obtain the unitary matrix U^ℓ that transforms the OAM matrix representatives $(L_\alpha^{\xi, \ell_\xi})^{(\ell)}$ in the spherical-harmonic basis into the OAM matrix representatives L_α^{ξ, ℓ_ξ} in the cubic-harmonic basis of our Wannier tight-binding model (Eq. (20)):

$$L_\alpha^{\xi, \ell_\xi} = U^\ell (L_\alpha^{\xi, \ell_\xi})^{(\ell)} (U^\ell)^\dagger, \quad \alpha \in \{x, y, z\}. \quad (27)$$

As shown in Table S1, our Wannier model contains s ($\ell = 0$), p ($\ell = 1$), d ($\ell = 2$), and f ($\ell = 3$) orbitals. Using the procedure detailed in Eqs. (20) through (27), we may now construct the OAM matrix representatives L_α required to compute $\langle \mathbf{L}(\mathbf{k}, E) \rangle$ in Eq. (19). For each of the orbital shells with $\ell \neq 0$ enumerated below, we will specifically provide explicit matrix representatives in the form of $(2\ell + 1) \times (2\ell + 1)$ square matrices, each of which is taken to be shorthand notation for a larger $N_L N_s (2\ell + 1) \times N_L N_s (2\ell + 1)$ matrix that is proportional to the identity in the $N_s N_L \times N_s N_L$ spin and layer subspace (Eq. (5)).

First, for the p shell of the $2d$ As atoms (denoted with $\xi, \ell_\xi \equiv (p)$), the real cubic harmonics are expressed in terms of the spherical harmonics Y_1^m as:

$$p_z = Y_1^0, \quad p_x = \frac{1}{\sqrt{2}} (Y_1^{-1} - Y_1^1), \quad p_y = \frac{i}{\sqrt{2}} (Y_1^{-1} + Y_1^1). \quad (28)$$

In the cubic-harmonic ordering $\{p_z, p_x, p_y\}$, the ladder operators $L_\pm^{(p)}$ in the Wannier basis are then represented by:

$$L_+^{(p)} = \begin{pmatrix} 0 & 1 & -i \\ -1 & 0 & 0 \\ i & 0 & 0 \end{pmatrix}, \quad L_-^{(p)} = \begin{pmatrix} 0 & -1 & -i \\ 1 & 0 & 0 \\ i & 0 & 0 \end{pmatrix}, \quad (29)$$

and the block 3×3 OAM representatives $L_\alpha^{(p)}$, $\alpha \in \{x, y, z\}$ in the Wannier basis are given by:

$$L_x^{(p)} = \begin{pmatrix} 0 & 0 & -i \\ 0 & 0 & 0 \\ i & 0 & 0 \end{pmatrix}, \quad L_y^{(p)} = \begin{pmatrix} 0 & -i & 0 \\ i & 0 & 0 \\ 0 & 0 & 0 \end{pmatrix}, \quad L_z^{(p)} = \begin{pmatrix} 0 & 0 & 0 \\ 0 & 0 & i \\ 0 & -i & 0 \end{pmatrix}. \quad (30)$$

Next, for the d shell of the $1a$ Eu atom (denoted with $\xi, \ell_\xi \equiv (d)$), the real cubic harmonics are expressed in terms of the spherical harmonics Y_2^m as:

$$\begin{aligned}
d_{z^2} &= Y_2^0, \\
d_{xz} &= \frac{1}{\sqrt{2}}(Y_2^{-1} - Y_2^1), \\
d_{yz} &= \frac{i}{\sqrt{2}}(Y_2^{-1} + Y_2^1), \\
d_{x^2-y^2} &= \frac{1}{\sqrt{2}}(Y_2^2 + Y_2^{-2}), \\
d_{xy} &= \frac{i}{\sqrt{2}}(Y_2^2 - Y_2^{-2}).
\end{aligned} \tag{31}$$

In the cubic-harmonic ordering $\{d_{z^2}, d_{xz}, d_{yz}, d_{x^2-y^2}, d_{xy}\}$, the ladder operators $L_\pm^{(d)}$ in the Wannier basis are then represented by:

$$L_+^{(d)} = \begin{pmatrix} 0 & 0 & -1 & -i & 0 \\ 0 & 0 & i & -1 & 0 \\ 1 & -i & 0 & 0 & -\sqrt{3} \\ i & 1 & 0 & 0 & \sqrt{3}i \\ 0 & 0 & \sqrt{3} & -\sqrt{3}i & 0 \end{pmatrix}, \quad L_-^{(d)} = \begin{pmatrix} 0 & 0 & 1 & -i & 0 \\ 0 & 0 & i & 1 & 0 \\ -1 & -i & 0 & 0 & \sqrt{3} \\ i & -1 & 0 & 0 & \sqrt{3}i \\ 0 & 0 & -\sqrt{3} & -\sqrt{3}i & 0 \end{pmatrix}, \tag{32}$$

and the block 5×5 OAM representatives $L_\alpha^{(d)}$, $\alpha \in \{x, y, z\}$ in the Wannier basis are given by:

$$L_x^{(d)} = \begin{pmatrix} 0 & 0 & 0 & -i & 0 \\ 0 & 0 & i & 0 & 0 \\ 0 & -i & 0 & 0 & 0 \\ i & 0 & 0 & 0 & \sqrt{3}i \\ 0 & 0 & 0 & -\sqrt{3}i & 0 \end{pmatrix}, \quad L_y^{(d)} = \begin{pmatrix} 0 & 0 & i & 0 & 0 \\ 0 & 0 & 0 & i & 0 \\ -i & 0 & 0 & 0 & \sqrt{3}i \\ 0 & -i & 0 & 0 & 0 \\ 0 & 0 & -\sqrt{3}i & 0 & 0 \end{pmatrix}, \quad L_z^{(d)} = \begin{pmatrix} 0 & 2i & 0 & 0 & 0 \\ -2i & 0 & 0 & 0 & 0 \\ 0 & 0 & 0 & i & 0 \\ 0 & 0 & -i & 0 & 0 \\ 0 & 0 & 0 & 0 & 0 \end{pmatrix}. \tag{33}$$

Lastly, for the f shell of the $1a$ Eu atom (denoted with $\xi, \ell_\xi \equiv (f)$), the real cubic harmonics are expressed in terms of the spherical harmonics Y_3^m as:

$$\begin{aligned}
f_{z^3} &= Y_3^0, \\
f_{xz^2} &= \frac{1}{\sqrt{2}}(Y_3^{-1} - Y_3^1), \\
f_{yz^2} &= \frac{i}{\sqrt{2}}(Y_3^{-1} + Y_3^1), \\
f_{z(x^2-y^2)} &= \frac{1}{\sqrt{2}}(Y_3^2 + Y_3^{-2}), \\
f_{xyz} &= \frac{i}{\sqrt{2}}(Y_3^2 - Y_3^{-2}), \\
f_{x(x^2-3y^2)} &= \frac{1}{\sqrt{2}}(Y_3^3 - Y_3^{-3}), \\
f_{y(3x^2-y^2)} &= \frac{i}{\sqrt{2}}(Y_3^3 + Y_3^{-3}).
\end{aligned} \tag{34}$$

In the cubic-harmonic ordering $\{f_{z^3}, f_{xz^2}, f_{yz^2}, f_{z(x^2-y^2)}, f_{xyz}, f_{x(x^2-3y^2)}, f_{y(3x^2-y^2)}\}$, the ladder operators $L_\pm^{(f)}$ in the

Wannier basis are then represented by:

$$L_+^{(f)} = \begin{pmatrix} 0 & \sqrt{6} & -\sqrt{6}i & 0 & 0 & 0 & 0 \\ -\sqrt{6} & 0 & 0 & \frac{\sqrt{10}}{2} & \frac{\sqrt{10}i}{2} & 0 & 0 \\ \sqrt{6}i & 0 & 0 & \frac{\sqrt{10}i}{2} & -\frac{\sqrt{10}}{2} & 0 & 0 \\ 0 & -\frac{\sqrt{10}}{2} & -\frac{\sqrt{10}i}{2} & 0 & 0 & \frac{\sqrt{6}}{2} & -\frac{\sqrt{6}i}{2} \\ 0 & -\frac{\sqrt{10}i}{2} & \frac{\sqrt{10}}{2} & 0 & 0 & -\frac{\sqrt{6}i}{2} & -\frac{\sqrt{6}}{2} \\ 0 & 0 & 0 & -\frac{\sqrt{6}}{2} & \frac{\sqrt{6}i}{2} & 0 & 0 \\ 0 & 0 & 0 & \frac{\sqrt{6}i}{2} & \frac{\sqrt{6}}{2} & 0 & 0 \end{pmatrix},$$

$$L_-^{(f)} = \begin{pmatrix} 0 & -\sqrt{6} & -\sqrt{6}i & 0 & 0 & 0 & 0 \\ \sqrt{6} & 0 & 0 & -\frac{\sqrt{10}}{2} & \frac{\sqrt{10}i}{2} & 0 & 0 \\ \sqrt{6}i & 0 & 0 & \frac{\sqrt{10}i}{2} & \frac{\sqrt{10}}{2} & 0 & 0 \\ 0 & \frac{\sqrt{10}}{2} & -\frac{\sqrt{10}i}{2} & 0 & 0 & -\frac{\sqrt{6}}{2} & -\frac{\sqrt{6}i}{2} \\ 0 & -\frac{\sqrt{10}i}{2} & -\frac{\sqrt{10}}{2} & 0 & 0 & -\frac{\sqrt{6}i}{2} & \frac{\sqrt{6}}{2} \\ 0 & 0 & 0 & \frac{\sqrt{6}}{2} & \frac{\sqrt{6}i}{2} & 0 & 0 \\ 0 & 0 & 0 & \frac{\sqrt{6}i}{2} & -\frac{\sqrt{6}}{2} & 0 & 0 \end{pmatrix}, \quad (35)$$

and the block 7×7 OAM representatives $L_\alpha^{(f)}$, $\alpha \in \{x, y, z\}$ in the Wannier basis are given by:

$$L_x^{(f)} = \begin{pmatrix} 0 & 0 & -\sqrt{6}i & 0 & 0 & 0 & 0 \\ 0 & 0 & 0 & 0 & \frac{\sqrt{10}}{2}i & 0 & 0 \\ \sqrt{6}i & 0 & 0 & \frac{\sqrt{10}}{2}i & 0 & 0 & 0 \\ 0 & 0 & -\frac{\sqrt{10}}{2}i & 0 & 0 & 0 & -\frac{\sqrt{6}}{2}i \\ 0 & -\frac{\sqrt{10}}{2}i & 0 & 0 & 0 & -\frac{\sqrt{6}}{2}i & 0 \\ 0 & 0 & 0 & 0 & \frac{\sqrt{6}}{2}i & 0 & 0 \\ 0 & 0 & 0 & \frac{\sqrt{6}}{2}i & 0 & 0 & 0 \end{pmatrix},$$

$$L_y^{(f)} = \begin{pmatrix} 0 & -\sqrt{6}i & 0 & 0 & 0 & 0 & 0 \\ \sqrt{6}i & 0 & 0 & -\frac{\sqrt{10}}{2}i & 0 & 0 & 0 \\ 0 & 0 & 0 & \frac{\sqrt{10}}{2}i & 0 & 0 & 0 \\ 0 & \frac{\sqrt{10}}{2}i & 0 & 0 & 0 & -\frac{\sqrt{6}}{2}i & 0 \\ 0 & 0 & -\frac{\sqrt{10}}{2}i & 0 & 0 & 0 & \frac{\sqrt{6}}{2}i \\ 0 & 0 & 0 & \frac{\sqrt{6}}{2}i & 0 & 0 & 0 \\ 0 & 0 & 0 & 0 & -\frac{\sqrt{6}}{2}i & 0 & 0 \end{pmatrix}, \quad L_z^{(f)} = \begin{pmatrix} 0 & 0 & 0 & 0 & 0 & 0 & 0 \\ 0 & 0 & i & 0 & 0 & 0 & 0 \\ 0 & -i & 0 & 0 & 0 & 0 & 0 \\ 0 & 0 & 0 & 0 & -2i & 0 & 0 \\ 0 & 0 & 0 & 2i & 0 & 0 & 0 \\ 0 & 0 & 0 & 0 & 0 & 0 & 3i \\ 0 & 0 & 0 & 0 & 0 & -3i & 0 \end{pmatrix}. \quad (36)$$

We have importantly confirmed by direct computation that the OAM matrix representatives L_α^{ξ, ℓ_ξ} in Eqs. (30) through (36) satisfy the canonical angular momentum commutation relations [87]:

$$[L_\alpha^{\xi, \ell_\xi}, L_\beta^{\xi, \ell_\xi}] = i \varepsilon^{\alpha\beta\gamma} L_\gamma^{\xi, \ell_\xi}, \quad (37)$$

where $\varepsilon^{\alpha\beta\gamma}$ is the Levi-Civita tensor and $\alpha, \beta, \gamma \in \{x, y, z\}$. We have also numerically confirmed that the L_α^{ξ, ℓ_ξ} matrices for each angular momentum shell satisfy the total angular momentum summation relation:

$$(L^{\xi, \ell_\xi})^2 = \sum_{\alpha=x,y,z} (L_\alpha^{\xi, \ell_\xi})^2 = \ell_\xi(\ell_\xi + 1) \mathbb{1}_{N_L N_s(2\ell_\xi+1) \times N_L N_s(2\ell_\xi+1)}, \quad (38)$$

where $\mathbb{1}_{N_L N_s(2\ell_\xi+1) \times N_L N_s(2\ell_\xi+1)}$ is the $N_L N_s(2\ell_\xi + 1) \times N_L N_s(2\ell_\xi + 1)$ identity matrix (see the text surrounding Eq. (20)).

Having established our OAM formalism, we may now finally compute the (001)-surface OAM texture ($\mathbf{L}(\mathbf{k}, E)$) (Eq. (19)) in our Wannier-based model of EuCd_2As_2 . In our CD-ARPES experiments, measurements were performed with the photon scattering plane aligned along the the (x, z) -plane of the sample (see Fig. 2b,d of the main text

and the Methods section). In momentum space, the photon scattering plane coincides with a crystallographic mirror plane whose normal vector lies along k_y and is related to the BZ line $\bar{\Gamma} - \bar{K}$ in Fig. S3a by crystal symmetry. We specifically employed in our CD-ARPES measurements 6 eV circularly polarized photons with bulk and surface sensitivity that were incident along an axis aligned 45° degrees between the x and z axes. We then extracted the CD-ARPES signature from the respective ARPES intensities $I_{CD} = I_{RCP} - I_{LCP}$. We hence interpret our CD-ARPES measurements as probing the $\langle L_{xz} \rangle = \langle \frac{L_x + L_z}{\sqrt{2}} \rangle$ component of the (001)-surface OAM texture. In Fig. S6c, we therefore plot $\langle L_{xz}(\mathbf{k}, E) \rangle$ for the Wannier-based model at the same constant energy as the overall surface spectral function $A_{\text{surf}}(\mathbf{k}, E)$ in Fig. S6a, using a signed log scale with a color map in which yellow is positive and dark blue is negative. The $\langle L_{xz}(\mathbf{k}, E) \rangle$ OAM texture component in Fig. S6c shows excellent agreement with our experimental CD-ARPES data measured at the same energy relative to the surface band minimum both above and below the PM to FM transition temperature $T_C \approx 25$ K (see Fig. S2c,d and the text following Eq. (16)).

Interestingly, unlike the $\langle S_{xz}(\mathbf{k}, E) \rangle$ spin texture component in Fig. S6b, $\langle L_{xz}(\mathbf{k}, E) \rangle$ in Fig. S6c exhibits the *same* sign for both concentric ring-like Fermi pockets of the surface Dirac cone. To demonstrate a scenario that qualitatively reproduces the spin and OAM textures in Fig. S6b,c, we introduce a simple $\mathbf{k} \cdot \mathbf{p}$ model $\mathcal{H}_{kp}(k)$ that represents a 1D line cut along k through a \mathcal{T} -invariant point $k = 0$ in a 2D surface BZ:

$$\mathcal{H}_{kp}(k) = k\tau_z + M\tau_x + v\tau_z\sigma_z. \quad (39)$$

In Eq. (39), there are four (surface-localized) basis states that arise from spin-degenerate $p_x \pm ip_y$ orbitals with the orbital magnetic quantum numbers (L_z eigenvalues) $m = \pm 1$ (see the text surrounding Eq. (21)), and hence overall form a total angular momentum $j = 3/2$ representation [87]. We employ a notation in Eq. (39) in which:

$$\tau_i\sigma_j = s_j \otimes s_i, \quad (40)$$

where s_i , $i \in \{x, y, z\}$ are the 2×2 Pauli matrices, s_0 is the 2×2 identity matrix, and where factors of τ_0 and σ_0 have been suppressed for notation simplicity. The matrices τ_z and σ_z respectively index the $p_x \pm ip_y$ orbital and spin-1/2 system subspaces, such that the matrix representatives of \hat{S}_z (Eq. (17)) and \hat{L}_z (Eq. (19)) are respectively given by:

$$S_z = \sigma_z, \quad L_z = \tau_z, \quad (41)$$

and \mathcal{T} symmetry is represented through the action:

$$\mathcal{T}\mathcal{H}_{kp}(k)\mathcal{T}^{-1} = \tau_x\sigma_y\mathcal{H}_{kp}^*(-k)\tau_x\sigma_y. \quad (42)$$

In $\mathcal{H}_{kp}(k)$ in Eq. (39), the velocity term $k\tau_z$ hence induces fully OAM-polarized dispersion kL_z , $M\tau_x$ is a \mathbf{k} -independent OAM coupling term that breaks L_z symmetry, and $v\tau_z\sigma_z$ is an S_z -symmetric SOC splitting term.

In Fig. S7, we respectively plot the total spectral function $A_{\text{surf}}(k, E)$ (Eq. (8), panels a,d,g in the top row), the $\langle S_z \rangle$ component of the spin texture $\langle \mathbf{S}(k, E) \rangle$ (Eq. (17), panels b,d,e in the middle row), and the $\langle L_z \rangle$ component of the OAM texture $\langle \mathbf{L}(k, E) \rangle$ (Eq. (19), panels c,f,i in the bottom row) as functions of E and k for $\mathcal{H}_{kp}(k)$ with varying values of M and v in Eq. (39). For all panels in Fig. S7, we have taken the top-surface projector P_t (Eq. (7)) to be the 4×4 identity matrix:

$$P_t = \mathbb{1}_{4 \times 4}, \quad (43)$$

because the low-energy Hamiltonian $\mathcal{H}_{kp}(k)$ is already projected into a (sub)space of surface-localized basis states.

We first in Fig. S7a,b,c plot $A_{\text{surf}}(k, E)$, $\langle S_z(k, E) \rangle$, and $\langle L_z(k, E) \rangle$ for $\mathcal{H}_{kp}(k)$ with $M = 0$ and $v = -0.05$. The spectral function $A_{\text{surf}}(k, E)$ in Fig. S7a consists of four linear bands with narrow spin splitting (Fig. S7b), where the bands within each spin-split pair exhibit $\langle L_z \rangle$ OAM polarizations with the same sign (Fig. S7c). Next, in Fig. S7d,e,f, we plot $A_{\text{surf}}(k, E)$, $\langle S_z(k, E) \rangle$, and $\langle L_z(k, E) \rangle$ for a case with vanishing SOC and significant OAM coupling in which $M = -0.1$ and $v = 0$. In this case, $A_{\text{surf}}(k, E)$ in Fig. S7d consists of two pairs of spin-degenerate bands with hyperbolic dispersion, for which $\langle S_z(k, E) \rangle$ is vanishing at all k due to the spin degeneracy (Fig. S7e). Importantly, however, the OAM texture $\langle L_z(k, E) \rangle$ in Fig. S7f remains nonvanishing, and the two doubly degenerate bands within each pair continue to exhibit the *same* sign of $\langle L_z \rangle$ at each k . We lastly consider the case of weakly introducing SOC into the previous scenario, and therefore in Fig. S7g,h,i plot $A_{\text{surf}}(k, E)$, $\langle S_z(k, E) \rangle$, and $\langle L_z(k, E) \rangle$ for $\mathcal{H}_{kp}(k)$ with $M = -0.1$ and $v = -0.05$. The energy spectrum in Fig. S7g now consists of two \mathcal{T} -enforced Dirac cones whose two branches are only weakly spin-split (Fig. S7h) and pairwise disperse in the same directions except at very small values of k . Specifically, focusing on the upper Dirac cone in energy in Fig. S7g, the two Dirac bands together form an essentially hyperbolic dispersion with positive velocities for all $k > 0$ outside of a very small momentum range in the vicinity of $k = 0$. This closely resembles the dispersion and spin texture distribution of the unoccupied (001)-surface states in our Wannier-based model of EuCd_2As_2 (Figs. S3b, S5a, and S6a,b). Also like the (001)-surface Dirac cone in

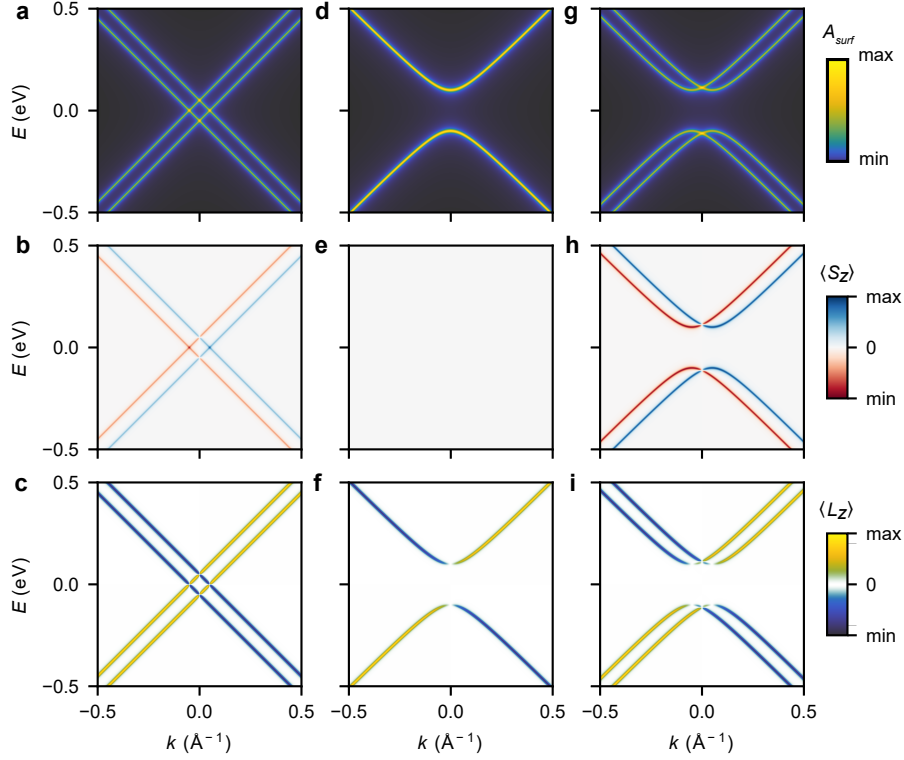


FIG. S7. Low-energy toy model of 2D Dirac surface states with contrasting spin and OAM polarizations: In this figure, we plot the spectral function $A_{\text{surf}}(k, E)$ (Eq. (8)), $\langle S_z(k, E) \rangle$ spin texture component (Eq. (17)), and $\langle L_z(k, E) \rangle$ OAM texture component (Eq. (19)) of a simplified, \mathcal{T} -invariant $\mathbf{k} \cdot \mathbf{p}$ model Hamiltonian $\mathcal{H}_{kp}(k)$ along a 1D line parameterized by k in a 2D surface BZ (Eqs. (39), (41), (42), and (43)). **(a, b, c)** $A_{\text{surf}}(k, E)$, $\langle S_z(k, E) \rangle$, and $\langle L_z(k, E) \rangle$, respectively, for $\mathcal{H}_{kp}(k)$ with $M = 0$ and $v = -0.05$. The spectrum in (a) consists of four linear bands with (b) narrow spin splitting, where the bands within each spin-split pair exhibit (c) $\langle L_z \rangle$ OAM polarizations with the same sign originating from the OAM dispersion term $k_z \tau_z = k L_z$ in Eqs. (39) and (41). **(d, e, f)** $A_{\text{surf}}(k, E)$, $\langle S_z(k, E) \rangle$, and $\langle L_z(k, E) \rangle$, respectively, for $\mathcal{H}_{kp}(k)$ with vanishing SOC and significant OAM coupling ($M = -0.1$, $v = 0$). The spectrum in (d) consists of two pairs of spin-degenerate bands with hyperbolic dispersion that (e) exhibit vanishing $\langle S_z \rangle$ at all k , due to the spin degeneracy, and (f) carry the same sign of $\langle L_z \rangle$ within each spin-degenerate pair. **(g, h, i)** $A_{\text{surf}}(k, E)$, $\langle S_z(k, E) \rangle$, and $\langle L_z(k, E) \rangle$, respectively, for the previous case in (d,e,f) subject to additional weak SOC ($M = -0.1$, $v = -0.05$). The spectrum in (g) consists of two \mathcal{T} -enforced twofold Dirac degeneracies at $k = 0$, where the bands from each Dirac point exhibit linear dispersion at small k , but otherwise largely follow the hyperbolic energy dispersion in (d). As in our Wannier-based calculations of the unoccupied (001)-surface states of EuCd_2As_2 (Fig. S6), the two singly degenerate branches of each Dirac cone in (g) exhibit (h) oppositely signed $\langle S_z \rangle$ spin polarizations, but (i) carry $\langle L_z \rangle$ OAM polarizations with the same sign.

our Wannier-based calculations (Fig. S6c), the two singly degenerate branches of each Dirac cone in Fig. S7i exhibit $\langle L_z \rangle$ OAM polarizations with the same sign, despite exhibiting oppositely signed $\langle S_z \rangle$ spin polarizations (Fig. S7h), owing to the dominant OAM dispersion term $k \tau_z = k L_z$ in Eqs. (39) and (41).

To conclude, we have introduced a simple $\mathbf{k} \cdot \mathbf{p}$ model that exhibits a 2D surface Dirac fermion with hyperbolic dispersion, weak spin splitting, and an OAM polarization distribution that mirrors our first-principles calculations of the (001)-surface spectrum of EuCd_2As_2 . It is important to note, however, that the simple model in Eq. (39) only represents a demonstration that it is feasible to realize a surface Dirac cone with these characteristics, and we leave for future works the more detailed question of the specific physical mechanism that gives rise to the (001)-surface energy dispersion and angular momentum textures in EuCd_2As_2 .

D. Topological classification and band topology above the Fermi level in EuCd_2As_2

In our calculations of the (001)-surface spectrum of the PM phase of EuCd_2As_2 in Secs. III B and III C, we observed (weakly SOC-split) 2D surface Dirac bands around $\mathbf{k} = \mathbf{0}$ with an energy minimum \tilde{E} above the Fermi level E_F (Figs. S3b, S5a, and S6). We will next investigate whether it is possible to associate the unoccupied Dirac surface

states in EuCd_2As_2 to bulk topological bands.

To address this question, we employ the approach of Ref. [15], in which the methods of Topological Quantum Chemistry [59, 82, 91] and symmetry-based indicators (SIs) [92–95] were applied to efficiently screen band structures in nonmagnetic materials (or material phases) at and away from E_F for nontrivial topology that is detectable from crystal symmetry eigenvalues. The authors of Ref. [15] specifically first performed DFT calculations using the Vienna Ab-initio Simulation Package (VASP) [96, 97], then applied the freely accessible Fortran program VASP2Trace (<https://github.com/zjwang11/irvsp>) [98] to extract the eigenvalues of the unitary crystal symmetries, and lastly uploaded the extracted symmetry eigenvalues to the Check Topological Mat tool on the Bilbao Crystallographic Server (BCS) to determine the band topology (accessible by navigating from <http://webbdcrista2.ehu.es/> to <https://cryst.ehu.es/cgi-bin/cryst/programs/magnetictopo.pl?tipog=gesp>) [99–102]. Because our DFT calculations in Sec. III A were performed using Quantum Espresso [40–42] and not VASP, we began by implementing custom code, detailed below, to extract the crystal symmetry eigenvalues from our band structure calculations in a format compatible with Check Topological Mat.

To construct an input file for Check Topological Mat from our DFT band structure calculation in Fig. S3a, we first analyzed nonmagnetic SG 164 ($P\bar{3}m1$), the 3D symmetry group G of EuCd_2As_2 in the PM state, to determine the set of maximal \mathbf{k} points (*i.e.* the \mathcal{T} -invariant \mathbf{k} points, as well as high-symmetry points without \mathcal{T} like K and H in Fig. S3a, see Refs. [59, 91]). At each maximal \mathbf{k} point, there specifically exists an infinite subgroup of symmetries $G_{\mathbf{k}} \subseteq G$, termed the little group, for which each symmetry:

$$g \in G_{\mathbf{k}}, \quad (44)$$

leaves \mathbf{k} invariant up to an integer linear combination \mathbf{K} of the reciprocal lattice vectors $\mathbf{b}_{1,2,3}$ in Eq. (2):

$$g\mathbf{k} \bmod \mathbf{K} = \mathbf{k}. \quad (45)$$

For each grouping of bands that share the same energy eigenvalue $E_{n\mathbf{k}}$ (up to a numerical tolerance factor of 0.002 eV), we next obtained the set of m (approximately) degenerate Bloch eigenstates $\{|\psi_{n\mathbf{k}}^1\rangle, |\psi_{n\mathbf{k}}^2\rangle, \dots, |\psi_{n\mathbf{k}}^m\rangle\}$ in an orthonormal basis. The m states that share the energy $E_{n\mathbf{k}}$ may either form an enforced degeneracy, or may simply be a set of states for which SOC and orbital splitting is very weak, but in either case transform into themselves or other degenerate states in the set under the action of the little group symmetries $g \in G_{\mathbf{k}}$ [91, 103].

Using the `spglib` software library [104], we then obtained a finite set of coset symmetry representatives with respect to the infinite group of translations for the full SG G , and restricted consideration to those that are also coset representatives of $G_{\mathbf{k}}$ using Eq. (45). Of the coset representatives of $G_{\mathbf{k}}$ obtained from `spglib`, a smaller subset consists only of unitary symmetries O , which hence carry eigenvalues that can be numerically obtained. Specifically, each unitary coset representative $O \in G_{\mathbf{k}}$ admits a decomposition of the form [103, 105]:

$$O = \{R|t\}, \quad (46)$$

where R is a point group operation and t is a (possibly fractional) translation. For the m (approximately) degenerate Bloch states with energy $E_{n\mathbf{k}}$, the action of the unitary little group symmetry O is represented by an $m \times m$ matrix $O^{\mathbf{k}}$:

$$O|\psi_{n\mathbf{k}}^i\rangle = \sum_{j=1}^m [O^{\mathbf{k}}]_{ij} |\psi_{n\mathbf{k}}^j\rangle, \quad (47)$$

where the matrix elements of $O^{\mathbf{k}}$ are hence given by:

$$[O^{\mathbf{k}}]_{ij} = \langle \psi_{n\mathbf{k}}^j | O | \psi_{n\mathbf{k}}^i \rangle. \quad (48)$$

In the plane-wave spinor basis of our DFT calculations, O in Eq. (46) acts by transforming \mathbf{k} vectors under R , multiplying by the phase factor $e^{-i(R\mathbf{k})\cdot t}$ from the combined action of R and t , and by applying the $\text{SU}(2)$ spin rotation that corresponds to the proper rotation piece of R . For each O and (approximate) band multiplet at $E_{n\mathbf{k}}$, we lastly obtain a character (trace) $\chi_{n\mathbf{k}}(O)$ by computing:

$$\chi_{n\mathbf{k}}(O) = \sum_{i=1}^m \langle \psi_{n\mathbf{k}}^i | O | \psi_{n\mathbf{k}}^i \rangle = \text{Tr } O^{\mathbf{k}}. \quad (49)$$

The characters $\chi_{n\mathbf{k}}(O)$ are equal to the sum of the symmetry eigenvalues of O for the m degenerate states at $E_{n\mathbf{k}}$, and across all maximal \mathbf{k} points and band degeneracies form a set of symmetry data vectors that can be used to determine band connectivity and topology [59, 91].

In Table S2, we reproduce the output from `Check Topological Mat` for the symmetry character trace file generated by our code (the tabulation of each $\chi_{n\mathbf{k}}(O)$ in Eq. (49)) applied to the DFT calculation of the PM-state electronic structure of EuCd_2As_2 in Sec. III A. The rows of Table S2 indicate groupings of connected bands above the core electronic shell, listed in the order realized by artificially, independently filling the Bloch states at each \mathbf{k} , rather than using a fixed, horizontal Fermi energy. This allows energetically isolated bands and gaps to be classified as “topological band insulators” that, while metallic in the bulk, still exhibit topological boundary states [82, 106]. In order, the columns in Table S2 list the irreducible small corepresentations associated to the characters $\chi_{n\mathbf{k}}(O)$ (Eq. (49)) at each maximal momentum \mathbf{k} in Fig. S3a, the total number of connected bands in the grouping including spin (dim), the classification of the bands in the language of Topological Quantum Chemistry (type, *e.g.* SEBR, see Ref. [15]), the symmetry indicators (SIs) ($Z_{2,3}, Z_4$) in SG 164 ($P\bar{3}m1$) of the energetically isolated bands (top. ind., respectively the $k_z = \pi$ weak \mathbb{Z}_2 invariant and the strong \mathbb{Z}_4 invariant), the cumulative band dimension realized by individually occupying each Bloch state up to an electronic filling ν above the core shell (filling ν), and the cumulative topology and SIs ($Z_{2,3}, Z_4$) of the symmetry-allowed gap at ν (all type / top. ind.). Most relevant to the present study of EuCd_2As_2 , $Z_4 \bmod 2$ in Table S2 corresponds to the Fu-Kane \mathbb{Z}_2 invariant for strong 3D topological insulating (TI) states [81, 107, 108], such that the rows with odd values of Z_4 in “all type / top. ind.” indicate electronic fillings at which topological surface Dirac cones may appear, modulo the effects of surface chemical potentials [15].

In the PM state, EuCd_2As_2 carries an intrinsic (valence) electronic filling above the core shell ν_F of:

$$\nu_F = 51. \quad (50)$$

Owing to the requirement from \mathcal{T} symmetry that noninteracting, nonmagnetic insulators have even numbers of occupied bands [66, 67], EuCd_2As_2 in the PM state is therefore, in the language of Ref. [15], an enforced semimetal with a Fermi degeneracy (ESFD) at $\nu = \nu_F$, and not a band insulator. The first gap in the PM state of EuCd_2As_2 allowed by symmetry instead occurs at a filling of $\nu = \nu_F + 1 = 52$ electrons, as indicated by the dashed horizontal line in Table S2. Remarkably, not only does the gap at $\nu = 52$ in EuCd_2As_2 carry the cumulative topology of a 3D TI state ($Z_4 = 3$ in “all type / top. ind.”), but in fact *all* of the symmetry-allowed band gaps realize 3D TI states over a range of $\Delta\nu = 12$ electrons spanning from $\nu = \nu_F - 5 = 46$ to $\nu = \nu_F + 7 = 58$. Hence, though surface chemical potentials may still shift topological surface Dirac cones away from the average energy of nontrivial band-insulating gaps (see the text following Eq. (14)), the huge filling range $\Delta\nu = 12$ of nontrivial 3D TI gaps surrounding ν_F in Table S2 is much larger than the scale of chemical potential effects, implying that the unoccupied (001)-surface Dirac cone in our DFT calculations (Figs. S3b, S5a, and S6) can be associated to a band-insulating 3D TI phase with $\nu \neq \nu_F$. Even further restricting to fillings above the Fermi energy $\nu > \nu_F$, it is also unlikely that surface chemical potential effects can shift a Dirac cone by energies equivalent to changing ν by 7 electrons, and we may hence more specifically reasonably associate the (001)-surface Dirac cone in Figs. S3b, S5a, and S6 to the smaller set of unoccupied 3D TI gaps with $\nu_F < \nu \leq 58$ in Table S2.

In this sense, EuCd_2As_2 is reminiscent of the repeat-topological (RTopo) materials introduced in Ref. [15], especially the example of Bi_2Mg_3 , which respects the same symmetry group SG 164 ($P\bar{3}m1$) as EuCd_2As_2 in the PM state. RTopo materials were specifically defined in Ref. [15] as materials that are stable topological band insulators at intrinsic filling ν_F , but also host cumulative stable topological band-insulating states at the first band gap below ν_F allowed by symmetry. In Bi_2Mg_3 , the RTopo classification gives rise to two sets of (001)-surface topological Dirac cones, which at intrinsic filling respectively manifest as surface states in the projected gap just above E_F , and as surface resonance bands below E_F that coexist with the surface projections of the bulk valence manifold and are associated to the topological band gap at $\nu < \nu_F$ [15–17]. If EuCd_2As_2 in the PM phase were doped to $\nu = \nu_F + 1 = 52$ (the dashed line in Table S2), it would also similarly be classified as RTopo. The unoccupied surface Dirac cone in EuCd_2As_2 (Figs. S3b, S5a, and S6) and the associated topological band gaps at $\nu > \nu_F$ in Table S2 can hence be viewed as a generalization of the concept of repeat-topology – originally introduced to predict topological boundary states accessible in equilibrium ARPES experiments at intrinsic filling – to topological surface conduction bands that are accessible by doping and pump-probe ARPES experiments like those in the present study.

Γ	A	H	K	L	M	dim	type	top. ind. ($Z_{2,3}, Z_4$)	filling ν	all type / top. ind. ($Z_{2,3}, Z_4$)
$\bar{\Gamma}_8(2)$	$\bar{A}_8(2)$	$\bar{H}_6(2)$	$\bar{K}_6(2)$	$\bar{L}_3\bar{L}_4(2)$	$\bar{M}_3\bar{M}_4(2)$	2	TRIVIAL	(0, 0)	2	TRIVIAL / (0, 0)
$\bar{\Gamma}_9(2)$	$\bar{A}_9(2)$	$\bar{H}_6(2)$	$\bar{K}_6(2)$	$\bar{L}_5\bar{L}_6(2)$	$\bar{M}_5\bar{M}_6(2)$	2	TRIVIAL	(0, 0)	4	TRIVIAL / (0, 0)
$\bar{\Gamma}_9(2)$	$\bar{A}_9(2)$	$\bar{H}_4\bar{H}_5(2)$	$\bar{K}_4\bar{K}_5(2)$	$\bar{L}_5\bar{L}_6(2)$	$\bar{M}_5\bar{M}_6(2)$	2	FRAGILE	(0, 0)	6	TRIVIAL / (0, 0)
$\bar{\Gamma}_6\bar{\Gamma}_7(2)$	$\bar{A}_6\bar{A}_7(2)$	$\bar{H}_6(2)$	$\bar{K}_6(2)$	$\bar{L}_5\bar{L}_6(2)$	$\bar{M}_5\bar{M}_6(2)$	2	FRAGILE	(0, 0)	8	TRIVIAL / (0, 0)
$\bar{\Gamma}_8(2)$	$\bar{A}_8(2)$	$\bar{H}_6(2)$	$\bar{K}_6(2)$	$\bar{L}_3\bar{L}_4(2)$	$\bar{M}_3\bar{M}_4(2)$	2	TRIVIAL	(0, 0)	10	TRIVIAL / (0, 0)
$\bar{\Gamma}_9(2)$	$\bar{A}_9(2)$	$\bar{H}_4\bar{H}_5(2)$	$\bar{K}_4\bar{K}_5(2)$	$\bar{L}_5\bar{L}_6(2)$	$\bar{M}_5\bar{M}_6(2)$	2	FRAGILE	(0, 0)	12	TRIVIAL / (0, 0)
$\bar{\Gamma}_4\bar{\Gamma}_5(2)$	$\bar{A}_4\bar{A}_5(2)$	$\bar{H}_6(2)$	$\bar{K}_6(2)$	$\bar{L}_5\bar{L}_6(2)$	$\bar{M}_5\bar{M}_6(2)$	2	SEBR	(1, 3)	14	SEBR / (1, 3)
$\bar{\Gamma}_6\bar{\Gamma}_7(2)$	$\bar{A}_6\bar{A}_7(2)$	$\bar{H}_6(2)$	$\bar{K}_6(2)$	$\bar{L}_3\bar{L}_4(2)$	$\bar{M}_5\bar{M}_6(2)$	2	SEBR	(1, 1)	16	TRIVIAL / (0, 0)
$\bar{\Gamma}_8(2)$	$\bar{A}_9(2)$	$\bar{H}_4\bar{H}_5(2)$	$\bar{K}_4\bar{K}_5(2)$	$\bar{L}_3\bar{L}_4(2)$	$\bar{M}_5\bar{M}_6(2)$	2	SEBR	(1, 0)	18	SEBR / (1, 0)
$\bar{\Gamma}_9(2)$	$\bar{A}_8(2)$	$\bar{H}_6(2)$	$\bar{K}_6(2)$	$\bar{L}_5\bar{L}_6(2)$	$\bar{M}_3\bar{M}_4(2)$	2	SEBR	(1, 0)	20	TRIVIAL / (0, 0)
$\bar{\Gamma}_8(2)$	$\bar{A}_8(2)$	$\bar{H}_6(2)$	$\bar{K}_6(2)$	$\bar{L}_5\bar{L}_6(2)$	$\bar{M}_3\bar{M}_4(2)$	2	SEBR	(1, 3)	22	SEBR / (1, 3)
$\bar{\Gamma}_9(2)$	$\bar{A}_9(2)$	$\bar{H}_6(2)$	$\bar{K}_6(2)$	$\bar{L}_3\bar{L}_4(2)$	$\bar{M}_5\bar{M}_6(2)$	2	SEBR	(1, 1)	24	TRIVIAL / (0, 0)
$\bar{\Gamma}_4\bar{\Gamma}_5(2)$	$\bar{A}_6\bar{A}_7(2)$	$\bar{H}_4\bar{H}_5(2)$	$\bar{K}_4\bar{K}_5(2)$	$\bar{L}_3\bar{L}_4(2)$	$\bar{M}_5\bar{M}_6(2)$	2	SEBR	(1, 0)	26	SEBR / (1, 0)
$\bar{\Gamma}_8(2)$	$\bar{A}_9(2)$	$\bar{H}_6(2)$	$\bar{K}_6(2)$	$\bar{L}_5\bar{L}_6(2)$	$\bar{M}_3\bar{M}_4(2)$	2	TRIVIAL	(0, 0)	28	SEBR / (1, 0)
$\bar{\Gamma}_6\bar{\Gamma}_7(2)$	$\bar{A}_4\bar{A}_5(2)$	$\bar{H}_6(2)$	$\bar{K}_6(2)$	$\bar{L}_5\bar{L}_6(2)$	$\bar{M}_3\bar{M}_4(2)$	2	SEBR	(1, 0)	30	TRIVIAL / (0, 0)
$\bar{\Gamma}_9(2)$	$\bar{A}_8(2)$	$\bar{H}_4\bar{H}_5(2)$	$\bar{K}_4\bar{K}_5(2)$	$\bar{L}_3\bar{L}_4(2)$	$\bar{M}_3\bar{M}_4(2)$	2	FRAGILE	(0, 0)	32	TRIVIAL / (0, 0)
$\bar{\Gamma}_8(2)$	$\bar{A}_9(2)$	$\bar{H}_4\bar{H}_5(2)$	$\bar{K}_4\bar{K}_5(2)$	$\bar{L}_3\bar{L}_4(2)$	$\bar{M}_3\bar{M}_4(2)$	2	SEBR	(1, 1)	34	SEBR / (1, 1)
$\bar{\Gamma}_8(2)$	$\bar{A}_8(2)$	$\bar{H}_6(2)$	$\bar{K}_6(2)$	$\bar{L}_5\bar{L}_6(2)$	$\bar{M}_5\bar{M}_6(2)$	2	SEBR	(1, 2)	36	SEBR / (0, 3)
$\bar{\Gamma}_4\bar{\Gamma}_5(2)$	$\bar{A}_8(2)$	$\bar{H}_6(2)$	$\bar{K}_6(2)$	$\bar{L}_3\bar{L}_4(2)$	$\bar{M}_5\bar{M}_6(2)$	4	FRAGILE	(0, 0)	40	SEBR / (0, 3)
$\bar{\Gamma}_9(2)$	$\bar{A}_4\bar{A}_5(2)$	$\bar{H}_6(2)$	$\bar{K}_6(2)$	$\bar{L}_3\bar{L}_4(2)$	$\bar{M}_3\bar{M}_4(2)$	4	FRAGILE	(0, 0)	42	SEBR / (0, 3)
$\bar{\Gamma}_9(2)$	$\bar{A}_9(2)$	$\bar{H}_4\bar{H}_5(2)$	$\bar{K}_4\bar{K}_5(2)$	$\bar{L}_5\bar{L}_6(2)$	$\bar{M}_5\bar{M}_6(2)$	2	FRAGILE	(0, 0)	44	SEBR / (0, 3)
$\bar{\Gamma}_6\bar{\Gamma}_7(2)$	$\bar{A}_6\bar{A}_7(2)$	$\bar{H}_6(2)$	$\bar{K}_6(2)$	$\bar{L}_5\bar{L}_6(2)$	$\bar{M}_3\bar{M}_4(2)$	2	SEBR	(0, 1)	44	TRIVIAL / (0, 0)
$\bar{\Gamma}_8(2)$	$\bar{A}_9(2)$	$\bar{H}_6(2)$	$\bar{K}_6(2)$	$\bar{L}_5\bar{L}_6(2)$	$\bar{M}_5\bar{M}_6(2)$	2	SEBR	(0, 3)	46	SEBR / (0, 3)
$\bar{\Gamma}_9(2)$	$\bar{A}_9(2)$	$\bar{H}_4\bar{H}_5(2)$	$\bar{K}_4\bar{K}_5(2)$	$\bar{L}_5\bar{L}_6(2)$	$\bar{M}_5\bar{M}_6(2)$	2	FRAGILE	(0, 0)	48	SEBR / (0, 3)
$\bar{\Gamma}_6\bar{\Gamma}_7(2)$	$\bar{A}_8(2)$	$\bar{H}_6(2)$	$\bar{K}_6(2)$	$\bar{L}_5\bar{L}_6(2)$	$\bar{M}_5\bar{M}_6(2)$	4	SEBR	(1, 0)	52	SEBR / (1, 3)
$\bar{\Gamma}_9(2)$	$\bar{A}_6\bar{A}_7(2)$	$\bar{H}_6(2)$	$\bar{K}_6(2)$	$\bar{L}_5\bar{L}_6(2)$	$\bar{M}_3\bar{M}_4(2)$	4	SEBR	(1, 0)	52	SEBR / (1, 3)

$\bar{\Gamma}_9(2)$	$\bar{A}_9(2)$	$\bar{H}_4\bar{H}_5(2)$	$\bar{K}_4\bar{K}_5(2)$	$\bar{L}_5\bar{L}_6(2)$	$\bar{M}_5\bar{M}_6(2)$	2	FRAGILE	(0, 0)	54	SEBR / (1, 3)
$\bar{\Gamma}_9(2)$	$\bar{A}_9(2)$	$\bar{H}_6(2)$	$\bar{K}_6(2)$	$\bar{L}_5\bar{L}_6(2)$	$\bar{M}_5\bar{M}_6(2)$	2	TRIVIAL	(0, 0)	56	SEBR / (1, 3)
$\bar{\Gamma}_6\bar{\Gamma}_7(2)$	$\bar{A}_6\bar{A}_7(2)$	$\bar{H}_6(2)$	$\bar{K}_6(2)$	$\bar{L}_5\bar{L}_6(2)$	$\bar{M}_5\bar{M}_6(2)$	2	FRAGILE	(0, 0)	58	SEBR / (1, 3)
$\bar{\Gamma}_9(2)$	$\bar{A}_9(2)$	$\bar{H}_6(2)$	$\bar{K}_6(2)$	$\bar{L}_3\bar{L}_4(2)$	$\bar{M}_5\bar{M}_6(2)$	2	SEBR	(1, 1)	60	TRIVIAL / (0, 0)

TABLE S2. **Symmetry data and topological classification from Check Topological Mat for the PM state of EuCd_2As_2 .** The output obtained from the Check Topological Mat tool on the Bilbao Crystallographic Server [15, 99–102] for the symmetry characters $\chi_{nk}(O)$ (trace file, see Eq. (49) and the surrounding text) from our DFT calculation of the electronic structure of EuCd_2As_2 in the PM state (SG 164 ($P\bar{3}m1$), see Sec. III A). The rows indicate groupings of connected bands above the core shell, listed in the order realized by independently filling the Bloch states at each \mathbf{k} . In order, the columns list the irreducible small corepresentations associated to the little group symmetry characters $\chi_{nk}(O)$ (Eq. (49)) at each maximal momentum \mathbf{k} in Fig. S3a, the total number of connected bands in the grouping including spin (dim), the classification of the bands in the language of Topological Quantum Chemistry (type, *e.g.* SEBR, see Ref. [15]), the symmetry-based indicators (SIs) of stable band topology ($Z_{2,3}, Z_4$) in SG 164 ($P\bar{3}m1$) for the energetically isolated bands (top. ind., respectively the $k_z = \pi$ weak Z_2 invariant and the strong Z_4 invariant), the cumulative band dimension realized by individually occupying each Bloch state up to an electronic filling ν above the core shell (filling ν), and the cumulative topology and SIs ($Z_{2,3}, Z_4$) of the symmetry-allowed gap at ν (all type / top. ind.). The columns “filling ν ” and “all type / top. ind.” are hence additive, and are obtained by respectively summing the data in the “dim” and “top. ind.” columns (including modulo operations for the cumulative SIs). Counting above the core shell, EuCd_2As_2 has $\nu_F = 51$ valence electrons (Eq. (50)), and is hence a \mathcal{T} -enforced metal in the PM state [66, 67] (ESFD in the nomenclature of Refs. [15, 102]). The first band gap allowed by symmetry above ν_F occurs at $\nu = \nu_F + 1 = 52$ (dashed horizontal line). The gap at $\nu = 52$, as well as all of the symmetry-allowed gaps from $\nu = \nu_F - 5 = 46$ to $\nu = \nu_F + 7 = 58$, exhibit the stable topology of a 3D topological insulator (TI), as indicated by their nontrivial Fu-Kane Z_2 invariants $Z_4 \bmod 2 = 1$ [81, 107, 108]. We may hence associate the unoccupied (001)-surface Dirac fermion in our DFT calculations of EuCd_2As_2 in Figs. S3b, S5a, and S6 to 3D TI gaps away from E_F , with the most likely candidates being the unoccupied topological band-insulating gaps at $\nu_F < \nu \leq 58$ (see the text following Eq. (50)).

IV. ESTIMATING THE POSITION OF THE BULK CONDUCTION BAND WITH ELECTRON ENERGY LOSS SPECTROSCOPY (EELS)

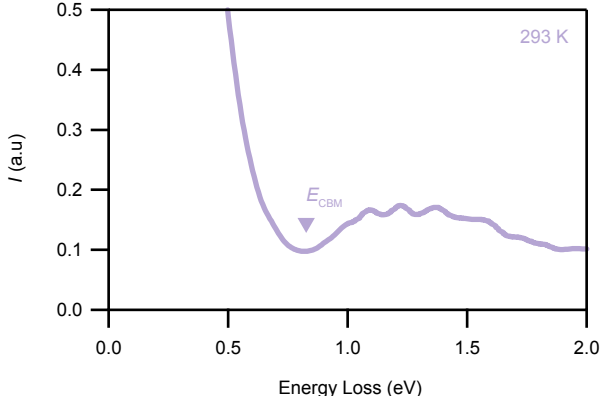


FIG. S8. **High-energy electron energy loss spectroscopy:** Momentum-integrated spectra obtained from electron energy loss spectroscopy (EELS), taken in the paramagnetic state of EuCd_2As_2 at 293 K. The local minimum near $E_{CBM} = E - E_F = 0.75 \text{ eV}$ that gives way to a broad continuum corresponds to the inter-band transition edge. The plasmon feature (Fig. 4b of the main text) lies above the vertical range of this plot.

Electron energy loss spectroscopy (EELS) measurements at low energies were presented in Fig. 4b of the main text, and showed a strong peak at approximately 0.12 eV, which we attribute to a plasmon. The EELS data at higher energies (Fig. S8) of the EuCd_2As_2 samples used in this study show a broad continuum of energy loss above $E_{CBM} = E - E_F = 0.75 \text{ eV}$, indicative of either a bulk or surface band minimum at that energy. In our first-principles electronic band structure calculations in Sec. III, we observe a bulk conduction band at approximately the same energy E_{CBM} (Fig. S3a). The value of $E_{CBM} = 0.75 \text{ eV}$ obtained from our EELS measurements is also in agreement with previous optical spectroscopy measurements on samples characterized as semimetallic [18], which place a conduction band minimum between 0.7 eV and 0.8 eV relative to the maximum of the hole-like valence band. Optical spectroscopy and Tr-ARPES studies of semiconducting samples [10] similarly place a local conduction band minimum at 0.8 eV.

V. EXTRACTING AND FITTING TRANSIENT ELECTRONIC TEMPERATURES AND DISPERSIONS FROM TR-ARPES DATA

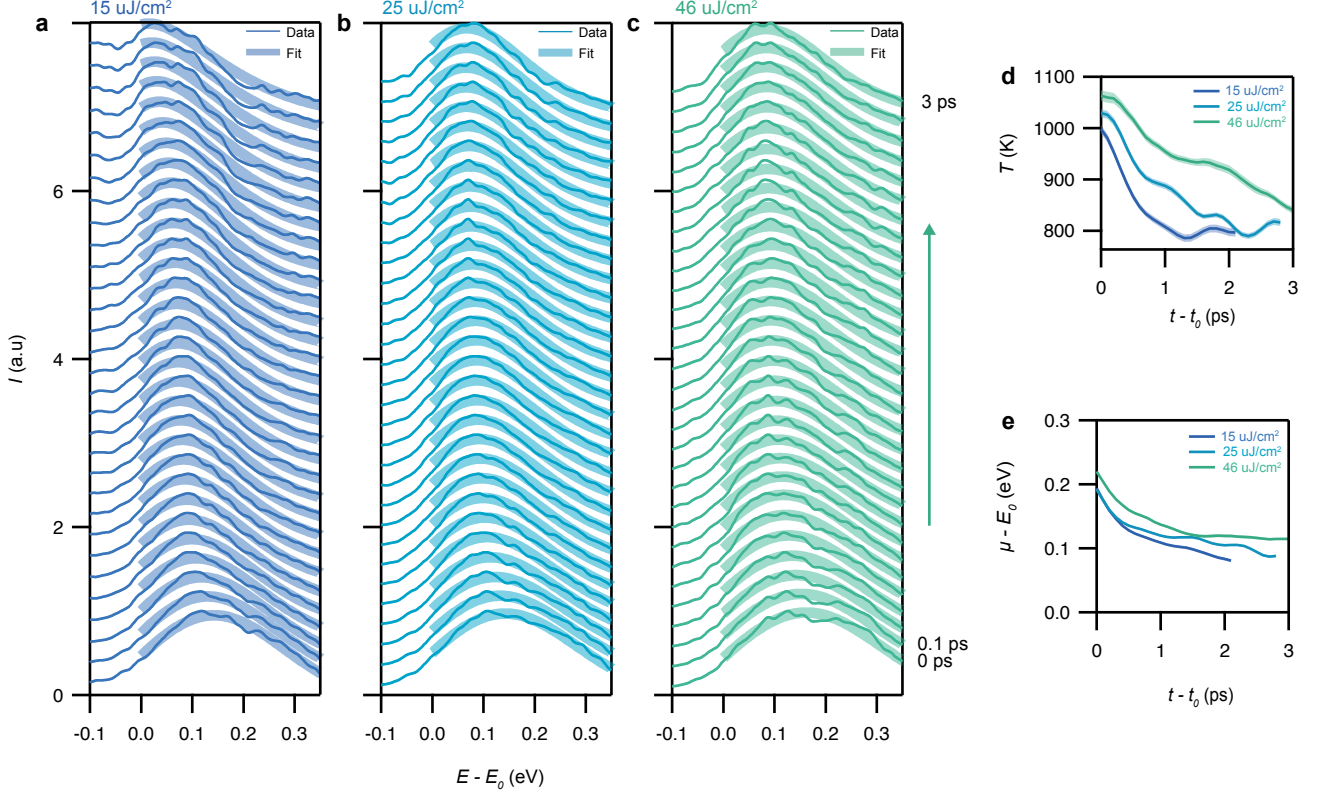


FIG. S9. **Waterfall plots for extracting time-dependent chemical potential and temperature from ARPES EDCs:** (a-c) Waterfall plots showing EDCs for the unoccupied surface states and corresponding fitted Fermi-Dirac distributions at time delays between 0 ps and 3 ps and energies measured relative to the bottom of the unoccupied surface state at $E_0 \approx E_F + 0.8$ eV. (d, e) Temperature (T) and chemical potential (μ) parameters extracted from the data in (a-c) as functions of time. Error bars for T and μ (the shaded regions in (a-c)) represent a 68% confidence interval for the fits.

We observe that under low-fluence excitation (below $46 \mu\text{J}/\text{cm}^2$), the momentum-integrated intensity of ARPES spectra are well-approximated at all times by a linear density of states multiplied by a Fermi-Dirac distribution, convolved with a fixed Gaussian energy resolution:

$$I(E, t) = A_0(t)(E - \alpha) \frac{1}{e^{(E - \mu(t))/k_B T(t)} + 1} * \text{Gauss}(E, \sigma = 10 \text{ meV}). \quad (51)$$

In Eq. (51), the parameter α is chosen to permit the presence of a nonzero density of states at E_0 , which we attribute to a rigid background due to either (or both) scattering from impurities and final state effects. These artifacts are independent of pump fluence and time after photo-excitation, and we therefore hold α constant at 0.05 eV.

In Fig. S9, we show the results of fitting EDCs at different times to the functional form of the ARPES intensity in Eq. (51). At high excitation fluences, we no longer employ Eq. (51). As described in the main text, under stronger excitation, we observe that the electronic distribution sharpens 100 meV above the bottom of the unoccupied surface state $E_0 \approx E_F + 0.8$ eV at increasing delay time after photo-excitation, which we attribute to the formation of excitons. The model of Eq. 51 is then no longer a reasonable physical description, since the excitons (specifically the electrons resulting from breaking excitons with the UV probe) would need to be ascribed their own statistical distribution. Lastly, we note that in Eq. (51), we have allowed the prefactor $A_0(t)$ to carry an explicit time dependence, because $A_0(t)$ scales with the total particle number in the unoccupied states, whose conservation is broken by significant radiative and impurity-mediated decay of electrons towards the equilibrium Fermi level.

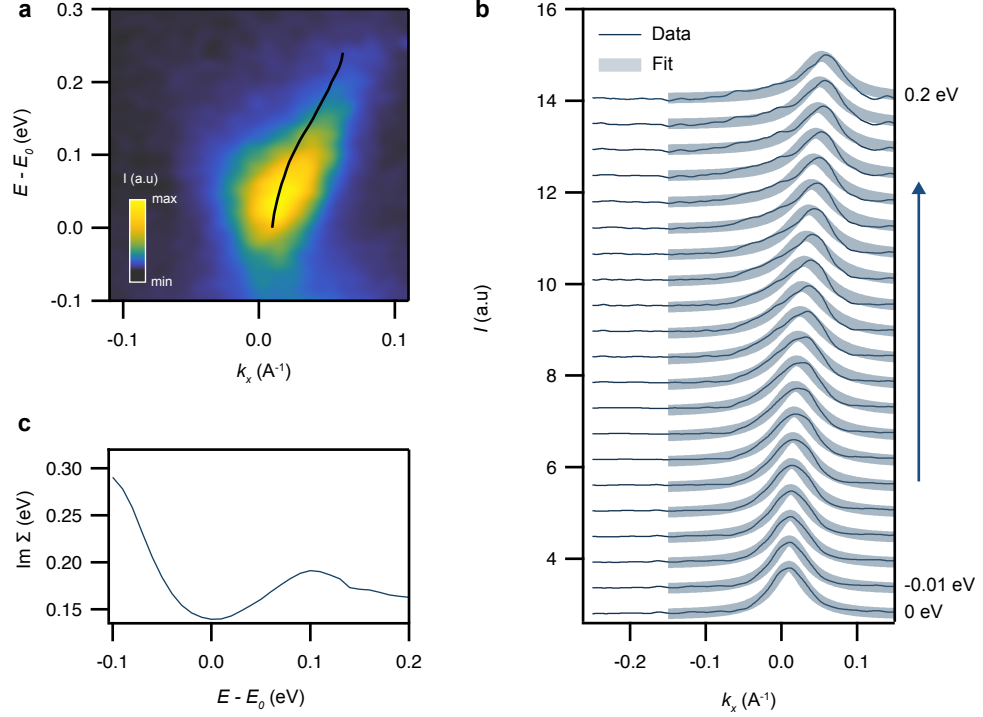


FIG. S10. **Waterfall plots for extracting dispersion from Lorentzian fits:** (a) Time-integrated ARPES spectrum for $t \in [0 \text{ ps}, 2 \text{ ps}]$ for low fluence excitation ($T = 14.5 \text{ K}$). The black line in (a) tracks the centers of Lorentzian fits of the momentum distribution curves (MDCs). (b) MDCs at several energy windows, with Lorentzian fits superimposed. (c) Example imaginary self energy $\text{Im } \Sigma(E)$ extracted from the half width at half maximum (HWHM) of the Lorentzian fits in (b).

In a one-band quasi-equilibrium system, the ARPES intensity can be written as [109, 110]:

$$I(k, E) = A(k, E) |M(k, E)|^2 f(E), \quad (52)$$

where $f(E)$ is the Fermi-Dirac distribution, $M(k, E)$ is a matrix element for the excitation of a bound electron to a plane-wave state, and $A(k, E)$ is the single-particle spectral function, given by:

$$A(k, E) = -\frac{1}{\pi} \frac{\Sigma''(k, E)}{[E - \epsilon(k) - \Sigma'(k, E)]^2 + [\Sigma''(k, E)]^2}. \quad (53)$$

In Eq. (53), $\epsilon(k)$ is a single-particle energy eigenvalue, and $\Sigma'(k, E) = \text{Re } \Sigma$ and $\Sigma''(k, E) = \text{Im } \Sigma$ are respectively the real and imaginary parts of the self energy, which are connected through the Kramers-Kronig relations. When Σ'' is taken to be independent of k (that is, scattering mechanisms encoded by Σ'' are assumed to vary slowly with momentum), cuts of $A(k, E)$ taken at constant E have a Lorentzian profile in k centered at $\epsilon(k) + \Sigma'(E)$ with a half width at half maximum (HWHM) proportional to Σ'' .

We therefore track the dispersion and imaginary self energy of the unoccupied surface states using Lorentzian fits of the MDCs. Our ARPES spectra were prepared by integrating over a short window starting at $t = t_0$, to account for rapid intra-band scattering and to allow significant spectral weight at all energy levels. As stated in the main text, there is no observed band renormalization; hence, the results of this fitting process are independent of our choice of the integration duration. Representative examples of an ARPES spectrum and a waterfall plot are displayed in Fig. S10, and show good agreement between individual cuts and the fits.

VI. ABSENCE OF TIME-DEPENDENT PHOTOVOLTAGE SHIFTS

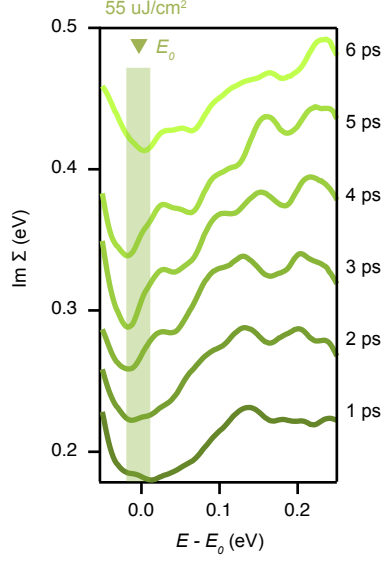


FIG. S11. **Time-dependence of photovoltage effects:** Plot of the imaginary self energy $\text{Im } \Sigma(E)$ at various delay times after $55 \mu\text{J}/\text{cm}^2$ excitation by 1.5 eV photons. Rigid vertical offsets have been added for clarity. Across all delay times, we observe no significant shift of the local minimum in $\text{Im } \Sigma(E)$ (green shaded region) relative to the bottom of the surface spectral feature at $E_0 \approx E_F + 0.8 \text{ eV}$. Details about the fitting process used to extract $\text{Im } \Sigma(E)$ from ARPES cuts are provided in Supplementary Information V.

In wide-gap semiconductors, it is well established that photovoltage effects can lead to shifts in the effective Fermi energy [4]. If present, this could shift the bottom of the surface spectral feature at $E_0 \approx E_F + 0.8 \text{ eV}$ upwards to E_X , leading to an apparent long-lived population at the middle of the dispersion extracted at $t \approx 0 \text{ ps}$. Such a rigid shift could additionally lead to time-dependent renormalization, similar to that observed in this work at high fluences in Fig. 3 of the main text.

To investigate photovoltage effects in our measurements, we track in Fig. S11 the position of the local minimum in the imaginary part of the self energy $\text{Im } \Sigma(E)$ of the unoccupied states, which necessarily appears at the bottom of the surface states, E_0 , as a function of delay time. Details about the fitting process used to extract $\text{Im } \Sigma(E)$ from ARPES cuts are provided in Supplementary Information V. This allows to us to address the possibility that the persistent population interpreted in this work as an exciton is instead simply an accumulation of electrons at the bottom of an unoccupied band. In Fig. S11, we importantly observe no significant time-dependent shift in the local minimum of $\text{Im } \Sigma(E)$, allowing us to exclude the trivial (non-excitonic) interpretation of our data.

VII. RATE EQUATION MODELING OF PLASMON-MEDIATED EXCITON FORMATION

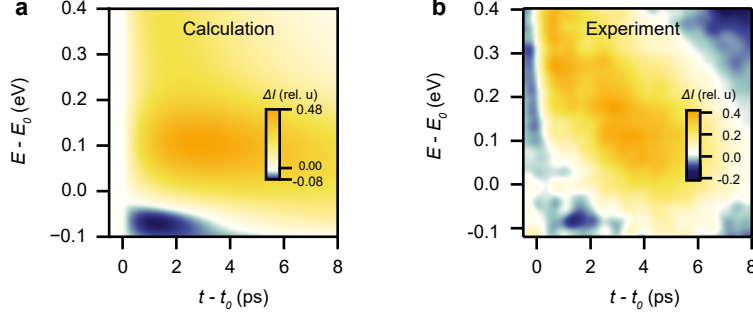


FIG. S12. **Theoretical modeling of plasmon-mediated exciton formation:** (a) Calculated and (b) observed difference between time traces for high and low fluence photo-excitation. The maximum population at each energy level was normalized to unity for each photo-excitation fluence. The calculation in (a) was obtained by using the parameters in Table S3 as input for $I_h(E, t) - I_\ell(E, t)$, where $I_\ell(E, t)$ and $I_h(E, t)$ are respectively defined in Eqs. (55) and (57). The experimental time trace data in (b) was acquired with fluences of 15 and 55 $\mu\text{J}/\text{cm}^2$.

Parameter	Value
Screened electron-plasmon coupling strengths at low fluence (α_ℓ)	1.7 $\text{ps}^{-1}\text{eV}^{-1}$
Screened electron-plasmon coupling strength at high fluence (α_h)	0.85 $\text{ps}^{-1}\text{eV}^{-1}$
Energy at which electronic lifetimes diverge (E_{CBM})	-0.1 eV
Impurity scattering time (τ_i)	25 ps
Exciton electron width (ς_X)	0.15 eV
Exciton hole width (ς_H)	0.075 eV
Exciton electron position (E_X)	0.1 eV
Exciton hole position (E_H)	-0.06 eV
Excitonic formation time (τ_{Xf})	2 ps
Excitonic lifetime (τ_{Xi})	6 ps
Excitonic spectral weight (A_X)	0.1

TABLE S3. Physical meaning and selected numerical values for the input parameters for our model of the electronic population dynamics in the unoccupied band structure (Fig. S12(a) and Eq. (57)). E_X , E_H , and E_{CBM} are measured relative to the bottom of the surface state, $E_0 \approx E_F + 0.8 \text{ eV}$.

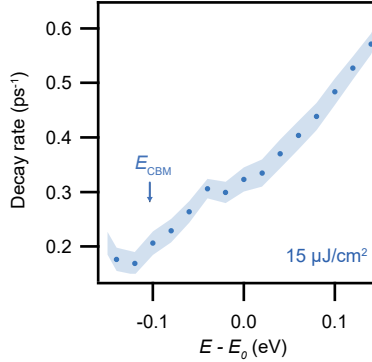


FIG. S13. Decay rate as a function of energy ($E - E_0$) for low fluence excitation (15 $\mu\text{J}/\text{cm}^2$), obtained from single exponential fits of Tr-ARPES data, which we use to estimate α_ℓ in Table S3 and Eq. (55). We additionally set $E_{CBM} = -0.1 \text{ eV}$, approximately where the decay rate reaches its minimum value. The shaded region represents a 68% confidence interval.

To evaluate whether the population dynamics presented in Fig. 5 of the main text are consistent with the proposed mechanism of plasmon-mediated exciton formation, we numerically model the population evolution using a rate

equation [111]. In Table S3, we list the physical meaning and selected values of the minimal parameters needed for this model.

The onset of the intensity at the instant of photo-excitation is approximately probe-limited (200 fs, see the Methods section of the main text). We hence treat the onset of the intensity at photo-excitation as a step function, given that the dynamics described above are significantly slower, and set observed intensities for both low and high excitation fluences to zero: $I_\ell(E, t < 0) = 0$ and $I_h(E, t < 0) = 0$. Below, we consider only $t \geq 0$.

We describe the electronic population $I_F^e(E, t)$ at a fluence F (with $F = \ell, h$ for low and high fluences respectively), energy E , and time t using

$$\frac{dI_F^e(E, t)}{dt} = -\bar{\alpha}_F(E) I_F^e(E, t), \quad (54)$$

where $\bar{\alpha}_F(E)$ is the effective energy-dependent scattering rate. For plasmon-mediated decay, we approximate $\bar{\alpha}_F(E) = \alpha_F(E - E_{CBM}) + \tau_i^{-1}$. The parameters α_ℓ and α_h in Table S3 respectively represent the screened electron-plasmon coupling strengths for the low fluence and high fluence cases. We treat the two cases as distinct due to screening effects and differences in the initial temperatures of the photo-doped population. We set α_ℓ to the slope of the graph of the decay rate over energy near E_0 for 15 $\mu\text{J}/\text{cm}^2$ photo-excitation (Fig. S13). τ_i is an energy-independent impurity-mediated scattering time. E_{CBM} is measured relative to the bottom of the surface state, $E_0 \approx E_F + 0.8 \text{ eV}$, and lies at the bottom of the broad energy range over which spectral weight from the bulk conduction band is observed (indicated by the yellow triangle in Fig.2c of the main text). It coincides with the energy of a bulk conduction band in our PM-state DFT calculation that is nondispersing at Γ to leading order (Fig. S3a). In Fig. S13, we confirm that the decay rate indeed reaches its minimum value at approximately E_{CBM} .

To eliminate effects associated with the density of states (which decreases observed spectral weight at lower energies) and the choice of excitation photon energy (which places an upper bound on the range of electronic energies that can be occupied), we normalize the maximum intensity at each energy level to unity. For low fluence excitation, when the re-absorption of plasmons by cooled electrons is negligible, the observed intensity $I_\ell(E, t)$ originates entirely from electrons, with no excitonic contribution, giving $I_\ell(E, t) = I_\ell^e(E, t)$. Thus, the energy-normalized spectral intensity can be written using Eq. (54) as:

$$I_\ell(E, t \geq 0) = \exp[-t(\alpha_\ell(E - E_{CBM}) + \tau_i^{-1})]. \quad (55)$$

For high fluence excitation, we add further terms to Eq. (55) to account for the arrival (along the timescale of exciton formation τ_{Xf}) and decay (along the timescale of the exciton lifetime τ_{Xl}) of electrons at E_X [32], as well as a corresponding term of opposite sign at E_H to account for the conservation of particle number (that is, hole formation). By this approach, we express the observed intensity as the sum of electronic and excitonic contributions:

$$I_h(E, t) = I_h^e(E, t) + I_h^X(E, t), \quad (56)$$

where $I_h^X(E, t)$ is positive (negative) at energies where the exciton's electron (hole) manifests in spectra. We assume the exciton electron and hole to have Gaussian spectral signatures with the respective standard deviations σ_X and σ_H , which are related to the full width half max (FWHM) $\varsigma_{E,H}$ of the corresponding features in the EDCs by $\sigma_{E,H} = \varsigma_{E,H}/(2\sqrt{2\log 2})$. E_X and E_H are measured relative to the bottom of the surface state, $E_0 \approx E_F + 0.8 \text{ eV}$, and are identified from normalized differences in time traces (see Fig. 5b of the main text, displayed without annotation in Fig. S12b). E_H is allowed to lie slightly above E_{CBM} , to match experimental data and avoid numerical divergences. Like E_{CBM} , E_H lies within the broad spectral weight associated with the bulk conduction band (Fig.2c of the main text). This results in a refinement of Eq. (55) given by:

$$\begin{aligned} I_h(E, t \geq 0) = & \exp[-t(\alpha_h(E - E_{CBM}) + \tau_i^{-1})] \\ & + \frac{A_X}{\sigma_X \sqrt{2\pi}} \exp\left(-\frac{(E - E_X)^2}{2\sigma_X^2}\right) \\ & \quad \left(1 - e^{-t/\tau_{Xf}}\right) e^{-t(\tau_{Xl}^{-1} + \tau_i^{-1})} \\ & - \frac{A_X}{\sigma_H \sqrt{2\pi}} \exp\left(-\frac{(E - E_H)^2}{2\sigma_H^2}\right) \\ & \quad \left(1 - e^{-t/\tau_{Xl}}\right) e^{-t(\tau_{Xf}^{-1} + \tau_i^{-1})}. \end{aligned} \quad (57)$$

The positive (negative) Gaussian term adds (removes) electronic spectral weight at E_X (E_H) due to breaking of the exciton during photoemission contributing an electron (hole) to the measured intensity.

Finally, in Fig. S12a, we plot $I_h(E, t) - I_\ell(E, t)$ using the parameter values in Table S3. The theoretical calculation in Fig. S12a shows good qualitative agreement with the corresponding experimental results in Fig. S12b.